Marginally Outer Trapped Surfaces in the Maximal Kruskal-Szekeres Extension

by

© **Liam Arthur Newhook**

A thesis submitted to the School of Graduate Studies in partial fulfillment of the requirements for the degree of Master of Science.

Department of Physics and Physical Oceanography

Memorial University

June 2024

St. John's, Newfoundland and Labrador, Canada

Abstract

For the last few decades and especially since the first detection of gravitational waves, black hole mergers have been a core research area in general relativity. However, the process by which two black hole horizons merge is only now starting to be well-understood. In numerical studies of apparent horizon evolution, self-intersecting marginally outer-trapped surfaces (MOTS) were found and play a key role [12]. Later a seemingly infinite number of self-intersecting MOTSs were found in Painlevé–Gullstrand slices of the Schwarzschild solution [4]. Further work has shown that their existence is robust and not simply an artifact of that coordinate system [11]. This thesis presents results found when examining the maximal extension to the Schwarzschild black hole in Kruskal-Szekeres coordinates. In this system, two separate universes dynamically connect through a worm-hole and pass through a moment of time-symmetry before the worm-hole pinches off and they disconnect. In these time slices, self-intersecting MOTS are found which, among other things, straddle the Einstein-Rosen bridge extending into both universes. Of particular interest is the stability analysis of the numerical solvers used, exotic toroidal surfaces, and the MOTS stability operator.

Lay Summary

Marginally Outer Trapped Surfaces, or MOTSs, are surfaces in which light can not expand or contract freely. These surfaces are found when examining black hole merger simulations and have been shown to exist when studying just one black hole [4]. In this work, I examine a time slicing of the Schwarzschild black hole which features a wormhole that connects two universes. I find exotic MOTSs that exhibit interesting behaviours, as well as examine and analyze the surfaces and the methods used to find them. This work aims to contribute to the understanding of black hole merger dynamics.

Acknowledgements

This work has been made possible due to a great network of supporters. My supervisor, Dr. Ivan Booth has been instrumental in the completion of this work, as the entirety of my understanding of General Relativity has come from his teaching. I also mention fellow researcher, and friend, Billy Sievers, who has provided council at many moments during the construction of this thesis. Section 2.8, as well as my understanding of numerical works, including numerical methods and stability analysis, has come from my time with Dr. Scott MacLachlan, who I greatly appreciate. Finally, I would not have been able to complete this work without the support of my cat Albert.

Statement of contribution

Portions of Chapters 3 and 4 are based on:

- Kam To Billy Sievers et al. Marginally Outer Trapped Tori in Black Hole Spacetimes. 2023. arXiv: 2312.00769 [gr-qc]

Author's contributions: The author made the discovery of the spherical non-enclosing MOTSs seen in Figures 10, 12, and 13. The author also co-wrote and ran the code that generated the results in sections 3 and 4, along with drafts contributing to the accompanying text. This thesis was written by the author.

Contents

List of Figures

Chapter 1

Introduction

1.1 The Marginally Outer Trapped Surface

To begin the discussion of the main subject of this thesis, I present the Hawking and Ellis pair of pants diagram in Figure 1.1 [10]. The diagram depicts a black hole merger, where time progresses as you move upwards. The outer-most surfaces, the "pair of pants", represent the event horizon. Initially the two black holes have their own distinct event horizons but when they get close enough, a common horizon is formed. The two inner tubes represent the apparent horizons, which end up inside a common apparent horizon near the top of the graph. Notice that this formation is discontinuous, while the event horizon is continuous. The apparent horizons are examples of Marginally Outer Trapped Surfaces, or MOTSs, which will be described within this section and the following one. The outer-most MOTS is the only necessarily *stable* MOTS [1]. Some time after the construction of this diagram, numerical simulations of black hole mergers showed that the inner MOTSs have some unexpected exotic behaviours during the mergers [13].

This numerical work led to the discovery of an exotic behaviour of these MOTSs,

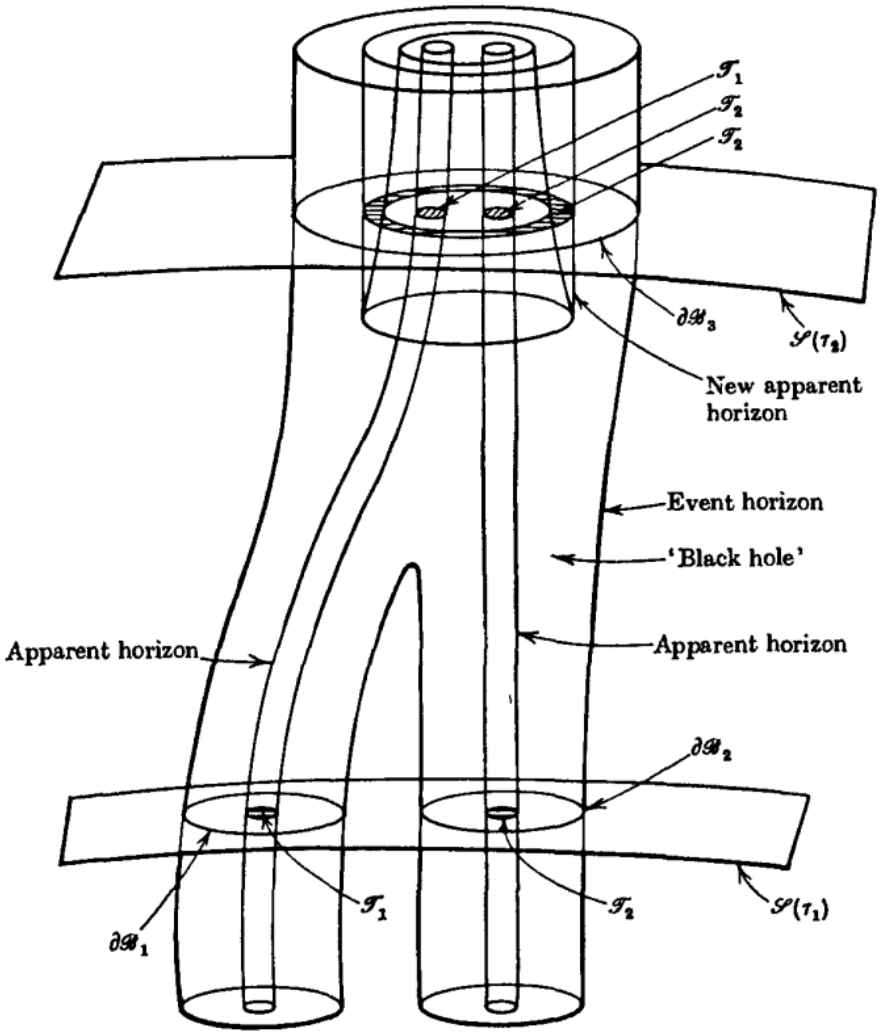

Figure 1.1: "Pair of pants" diagram from Hawking and Ellis [10] page 322. Figure depicts black hole merger.

the self-intersection shown in the right-most plot of Figure 1.2. This led to further studies and it was found that these surfaces not only exist when considering a merger of two black holes, but also when studying just one black hole [4]. This was done by considering a Schwarzschild black hole in Painlevé-Gullstrand coordinates (1.1). These coordinates are generated by infalling timelike geodesics and have no coordinate singularity at the outer horizon of the black hole. This can be seen just by looking

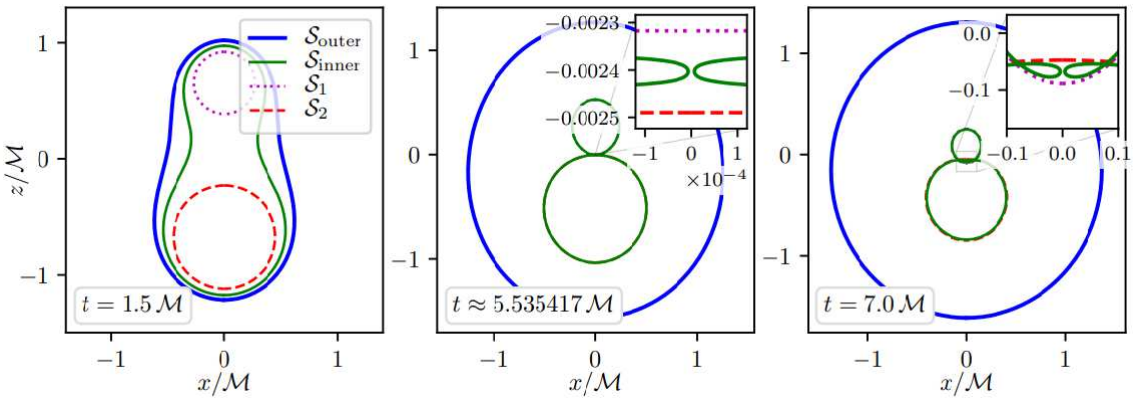

Figure 1.2: Black hole merger simulation with outer common formed horizon being denoted by solid blue line. Dashed lines are the original outer horizons of each black hole. Solid green line is MOTS formed when black holes get close enough. Notice self-intersection during overlap of original horizons. Figure taken from page 4 of [13].

at the metric (1.1) and noticing there is no divergence at $r = 2M$,

$$ds^2 = -\left(1 - \frac{2M}{r}\right)d\tau^2 + 2\sqrt{\frac{2M}{r}}d\tau dr + dr^2 + r^2(d\theta^2 + \sin^2\theta\phi^2). \tag{1.1}$$

In this study, it was found that there are an apparently infinite number of these self-intersecting MOTSs, several of these surfaces are shown in Figure 1.3.

With this discovery, the doors for a larger study of these surfaces in many other spacetimes were opened. This thesis was specifically the result of studying these surfaces in time slices of the Kruskal-Szekeres coordinates that will be described in the next chapter. The main reason for studying these slices is because toroidal surfaces were found in the merger simulations but not in any of the studied spacetimes such as Painlevé-Gullstrand [4]. $T = 0$ time slices of Schwarzschild in the Kruskal-Szekeres coordinates have similar geometric properties to the initial time slices of these merger spacetimes, so this research began with the hope of understanding if the toroidal

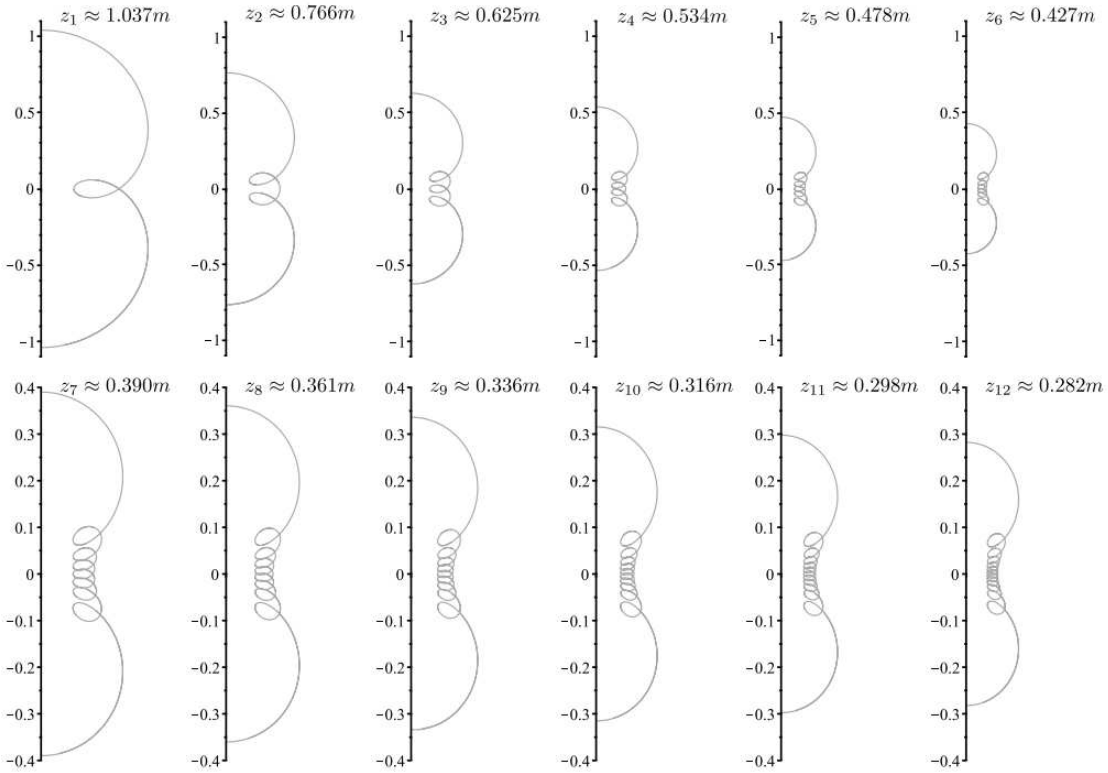

Figure 1.3: Many N-looping self-intersecting MOTSs from finding surfaces in Painlevé-Gullstrand coordinates. Figure is taken from page 11 of [4].

surfaces are a result of the mergers or the initial conditions.

I will now proceed to describe the building blocks of the MOTS. This discussion will begin with short descriptions of special and general relativity and end with a derivation of the equations needed to find MOTS. This will be followed by a presentation of all results found during the course of this research, beginning with self-intersecting MOTSs and ending with toroidal MOTSs. Finally, a discussion of the stability operator will be had before ending with a conclusion.

Chapter 2

Background

General relativity has been a blossoming area of research since its formulation by Einstein [7]. The theory provided the mathematical language to describe not only the ultra-massive, but near-speed-of-light regimes. While our classical understanding of gravity may be able to comfortably handle the mundane, relativity is required where the extremes of mass and velocity come into question. This gap between these views of the world is demonstrated by showcasing the Lorentz transformations [16]. These transformations are a way to describe how physics is understood from one frame to another. In Einstein's papers [7] he made use of these transforms to showcase that at relative speeds near c, the speed of light, time dilation and length contractions would be apparent.

2.1 Special Relativity

Consider the rod example from Einstein's papers. Many people within science will have heard this at least once before. A depiction of this example is shown in Figure 2.1. Suppose a rod sits along an axis x' in some reference frame K', with its back

end at the origin and its front end at a point I. We wish to know how a stationary observer measures its length relative to some reference frame K. Note that for the duration of this work, the speed of light will be set to the variable c.

Under a Lorentz transformation

$$x_f = I\sqrt{1 - \frac{v^2}{c^2}}, \tag{2.1}$$

where x_f is the rod end in the K' reference frame. From equation (2.1) it is clear that the length of the rod can be described as $I\sqrt{1 - \frac{v^2}{c^2}}$ meaning that with v being the observed velocity of the rod by the observer in K, the rod's length is contracted as velocities increase. It can also be noted that c is a limiting factor here as when we consider $v > c$ we begin having imaginary results. Classical physics does not show these results. In fact, it is straightforward to see that under Galilean transforms, the classical counterpart to Lorentz transforms, there are frames in which objects can have speeds greater than c. This violates Einstein's postulates and ultimately demonstrates the requirement for relativity in such systems.

2.2 General Relativity

While we have just described what is known as special relativity, this is sufficient to demonstrate that classical physics cannot describe all systems. We now proceed to describing general relativity. To begin, let us start with Einstein's equation [9]:

$$R_{\alpha\beta} - \frac{1}{2}g_{\alpha\beta}R = 8\pi G T_{\alpha\beta}. \tag{2.2}$$

We see here Einstein's relation of spacetime curvature to a measure of mass-energy. $R_{\alpha\beta}$ is the Ricci curvature, which describes spacetime curvature. The $T_{\alpha\beta}$ is the stress-

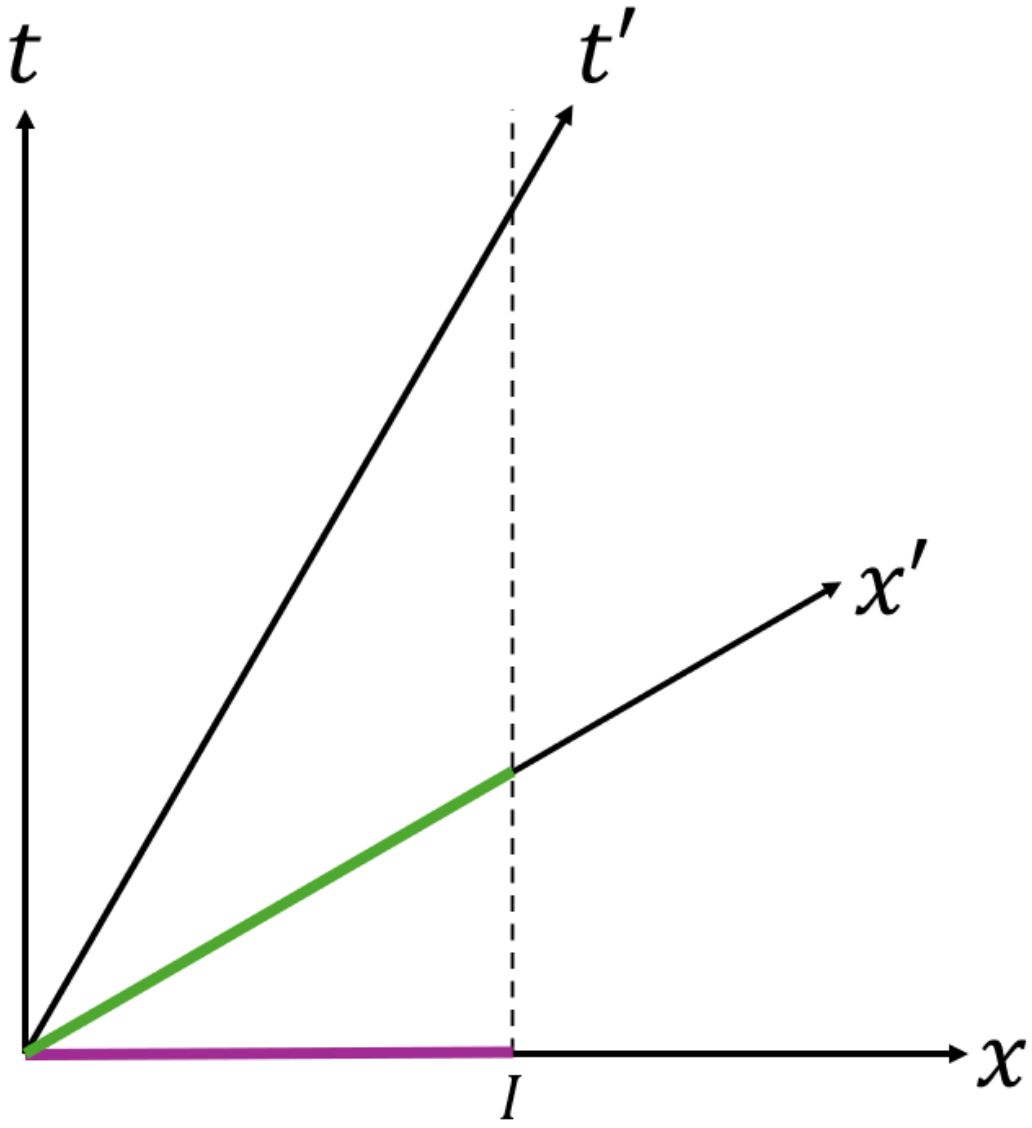

Figure 2.1: Diagram of length contraction example in special relativity. The purple line is the rod as seen by a stationary observer. The green line is the rod as seen by an observer moving at some relativistic speed. As is seen in the diagram, the rods length is contracted.

energy tensor, which describes matter energy-density-momentum. Note that in (2.2) $c = 1$. If a vacuum system is considered, $T_{\alpha\beta} = 0$ everywhere in the system. If this

is the case, then it can be shown that $R_{\alpha\beta}$ also reduces to zero. Consider then the following relation,

$$R_{\alpha\beta} - \frac{1}{2} g_{\alpha\beta} R = 0. \tag{2.3}$$

Contracting both sides of (2.3) by the inverse metric $g_{\alpha\beta}$ results in R having to be zero when the stress-energy T is zero. In turn this implies that $R_{\alpha\beta} = 0$. It is important to note that this equation is specifically the communication bridge between matter and the curvature of spacetime. I shall now proceed with a discussion of coordinates.

To begin the discussion of how spacetimes are mapped and measured, let us consider the line element. A line element defines the geometry of a spacetime, specifically offering a description of the distance between two nearby points within a spacetime. This then is a tool that allows for the taking of measurements within some given spacetime. Let us first consider a simple example of line elements, the flat Minkowski spacetime, which takes the following form,

$$ds^2 = -dt^2 + dx^2 + dy^2 + dz^2. \tag{2.4}$$

Note here that equation (2.4) is not *unique* in the sense that this is not the only possible line element describing flat space. One could also do a coordinate transformation on equation (2.4) which will result in the same spacetime, just in different coordinates. Also note here the negative time signature, which means the components of the line element follow a signature of the form $(-, +, +, +)$.

The following relations can be used to perform a coordinate transformation,

$$
\begin{aligned}
x &= r\sin(\theta)\cos(\phi) \\
y &= r\sin(\theta)\sin(\phi) \\
z &= r\cos(\theta).
\end{aligned} \tag{2.5}
$$

Consider using the transformations (2.5) on equation (2.4). This will result in the following metric,

$$
ds^2 = -dt^2 + dr^2 + r^2 d\theta^2 + r^2\sin^2\theta d\phi^2. \tag{2.6}
$$

This is Minkowski space in spherical coordinates. Ultimately, these line elements take the following general form [2],

$$
ds^2 = g_{ab}dx^a dx^b. \tag{2.7}
$$

By introducing coordinates we have performed a key component of relativity, splitting space and time. Rewriting (2.7), one may see a very important component of such things, the metric g_{ab} relative to a choice of spacelike foliation,

$$
g_{ab} = \begin{pmatrix} -\alpha^2 + \beta_l\beta^l & \beta_i \\ \beta_j & \gamma_{ij} \end{pmatrix} \tag{2.8}
$$

where i, j, l are indices running across the space coordinates. Equation 2.8 can be inverted to show the following,

$$
g^{ab} = \gamma^{ab} - n^a n^b. \tag{2.9}
$$

Here γ is the spatial metric which describes all components of the metric aside from the time components, and n is the normal to the surface. There are plenty of components of the metric definitions (2.8) and (2.9) that need some description. I shall start with the α and β shown in equation (2.8). These are the lapse and shift functions. The lapse describes how the coordinate time moves relative to proper time while the shift describes how some defined coordinates move through the spacetime. Essentially, these components are analogous to gauge choices in electricity and magnetism [2].

I make use of Figure 2.2 for the description of the lapse and shift. There is shown some hypersurface of a spacetime. This is a purely spacelike entity that we say is a "time slice" of our spacetime. This is to say that if we describe our spacetime with some coordinates, say (t, r, θ, ϕ), the hyper-surface Σ is described with some constant t, and coordinates (r, θ, ϕ). Imagining that one begins at some slice Σ_1 with some observer positioned on the slice with coordinates x_i, it will be seen that the lapse α will move through the spacetime normal to the surface and will control how far in time we move through the spacetime. The shift β then defines how the originally defined coordinates x_i change relative to movement through the spacetime. It is also noted that while considering the definition of the metric (2.8), it is seen that that along with the spatial metric γ_{ij}, which is just the metric without any of the time components, the lapse and shift describe the coordinates and how they move through spacetime.

2.3 Schwarzschild

Let us then move forward to very important work done by Schwarzschild, specifically his original solution to the problem of solving Einstein's equations for a spherically

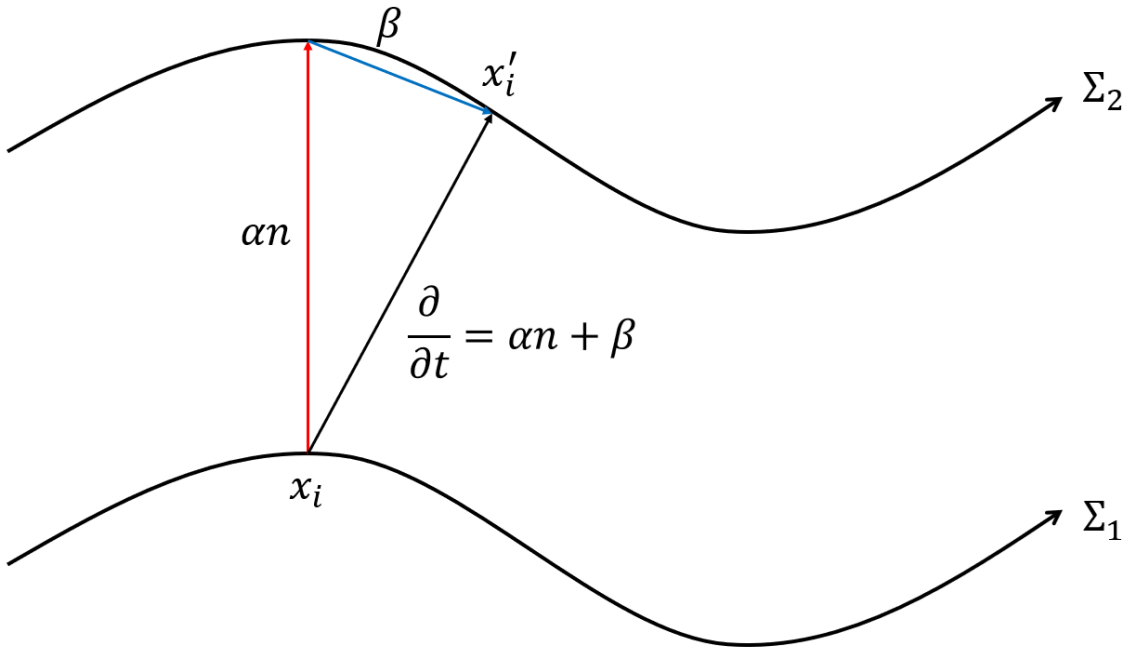

Figure 2.2: Diagram of how lapse α and shift β progress through some spacetime. With the lapse controlling how far in time you move and the shift controlling how the originally defined coordinates change as you move. Note here that the diagram labels are slightly misleading, but give a good description of how these entities behave.

symmetric source [14]. If considering one of the general metric descriptions above, specifically (2.8), the Schwarzschild metric can be written as

$$g_{ab} = \begin{pmatrix} -(1-\frac{2M}{r}) & 0 & 0 & 0 \\ 0 & (1-\frac{2M}{r})^{-1} & 0 & 0 \\ 0 & 0 & r^2 & 0 \\ 0 & 0 & 0 & r^2\sin^2\theta \end{pmatrix} \tag{2.10}$$

This definition (2.10) can be written in the line element form as:

$$ds^2 = -\left(1 - \frac{2M}{r}\right) dt^2 + \left(1 - \frac{2M}{r}\right)^{-1} dr^2 + r^2(d\theta^2 + \sin^2\theta d\phi^2). \tag{2.11}$$

The original solution [14] here was derived by Schwarzschild while he served during World War One. The solution describes a spherically symmetric non-rotating black hole with no charge. Notice here that the line element of a sphere of radius r embedded in three-dimensional space (2.12) [9] is contained within the line element of (2.11) and takes the form

$$d\Sigma^2 = r^2(d\theta^2 + \sin^2\theta d\phi^2). \tag{2.12}$$

As noted in [9], the r coordinate here is not the distance from some defined center but instead is defined by the area of the corresponding two-dimensional sphere of fixed r and t. This relation takes the form

$$r = \sqrt{\frac{A}{4\pi}}. \tag{2.13}$$

In these equations I have chosen units for G and c such that both are equal to one so that equations like (2.11) take a cleaner form.

Consider then the coefficients to dt^2 and dr^2 of equation (2.11). These terms both have an r in the denominators, meaning there is the expected singularity at $r = 0$. However, consider the dr^2 term again. Notice that this also diverges at $r = 2M$. This is specifically the horizon of the Schwarzschild black hole, at which our coordinates evidently break down.

2.4 Penrose-Carter Diagrams

A convenient way of picturing these spacetimes is using Penrose-Carter diagrams. Before engaging deeper into the Schwarzschild spacetime, let us take a step back and review how these diagrams work.

First, consider the flat spacetime defined by (2.6). If one wishes to construct a line element based on radial light rays moving along some defined constant lines u or v [9], then it is necessary to define these variables as $u = t - r$ and $v = t + r$. Plugging these definitions into (2.6) results in the following line element,

$$ds^2 = -du\ dv + \frac{(u-v)^2}{4}(d\theta^2 + \sin^2\theta d\phi^2). \tag{2.14}$$

Notice that from equation (2.14) and Figure 2.3, t and r have domains $-\infty < t < \infty$ and $0 < r < \infty$. To complete the work that will lead us to a true Penrose-Carter diagram we make another two transformations. The first compactifies the u and v coordinates into finite ranges $(-\frac{\pi}{2}, \frac{\pi}{2})$:

$$\begin{aligned} u' &= \tan^{-1} u \\ v' &= \tan^{-1} v \end{aligned} \tag{2.15}$$

and the second returns to Cartesian-like coordinates:

$$\begin{aligned} t' &= u' + v' \\ r' &= v' + u'. \end{aligned} \tag{2.16}$$

Thus, the infinite coordinates t and r have been mapped to finite coordinates t' and

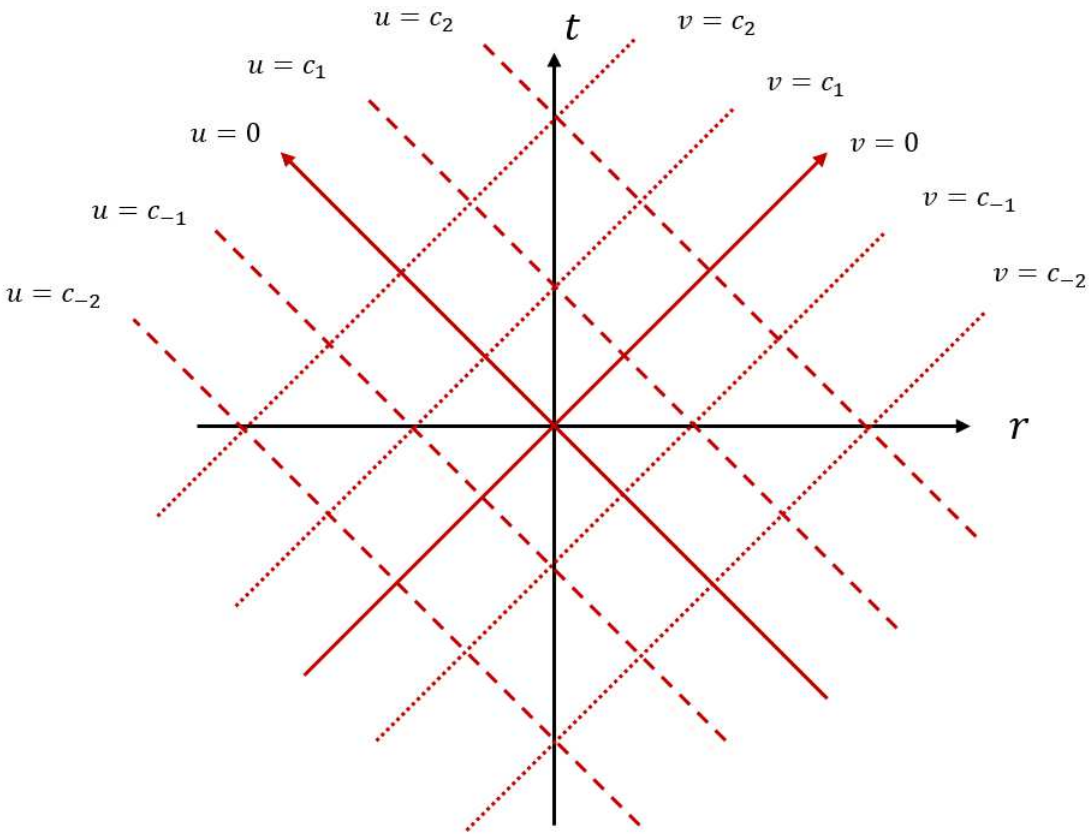

Figure 2.3: Diagram of spherical flat space with transformations $u = t - r$ and $v = t + r$. Line of constant u or v are the paths that light rays travel upon.

r', allowing for the construction of the Penrose-Carter diagram for flat space.

Consider now the finished Penrose-Carter diagram in Figure 2.4. This diagram demonstrates key properties of Minkowski space. Specifically the coordinates are constructed such that there are now null, timelike, and spacelike infinities all defined on the diagram. The $\mathscr{I}_+$ and $\mathscr{I}_-$ denote the future and past null infinities ($t' + r' = \pi, r' - t' = \pi$), while I_+ and I_- denote the timelike infinities ($t' = \pi$). I_0 then denotes spacelike infinity ($r' = \pi$). The benefit of mapping this way is that one can now depict a plethora of things, such as how light travels within the depicted spacetime.

An example of a useful attribute of the Penrose-Carter diagrams is shown in Figure

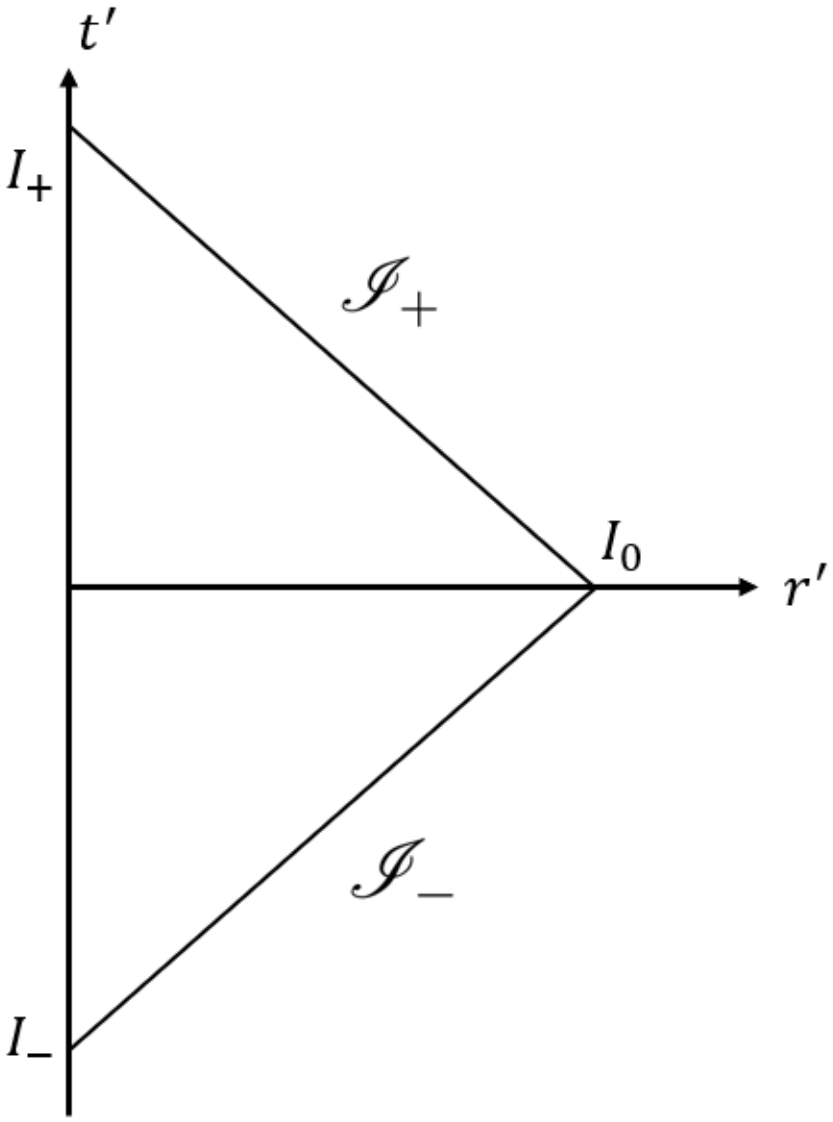

Figure 2.4: Penrose-Carter diagram of spherical flat space. Noting here that $\mathscr{I}_+$ and $\mathscr{I}_-$ are the future and past null infinities. I_+, I_-, and I_0 are future timelike infinity, past timelike infinity, and spacelike infinity respectively.

2.5, where an observer $\mathscr{B}$ is placed at the black dot, somewhere in the spacetime. From the diagram, it is noted that 45° lines are lines in which light travels, which are the radial null geodesics. The shaded region shown below observer $\mathscr{B}$ denotes the region

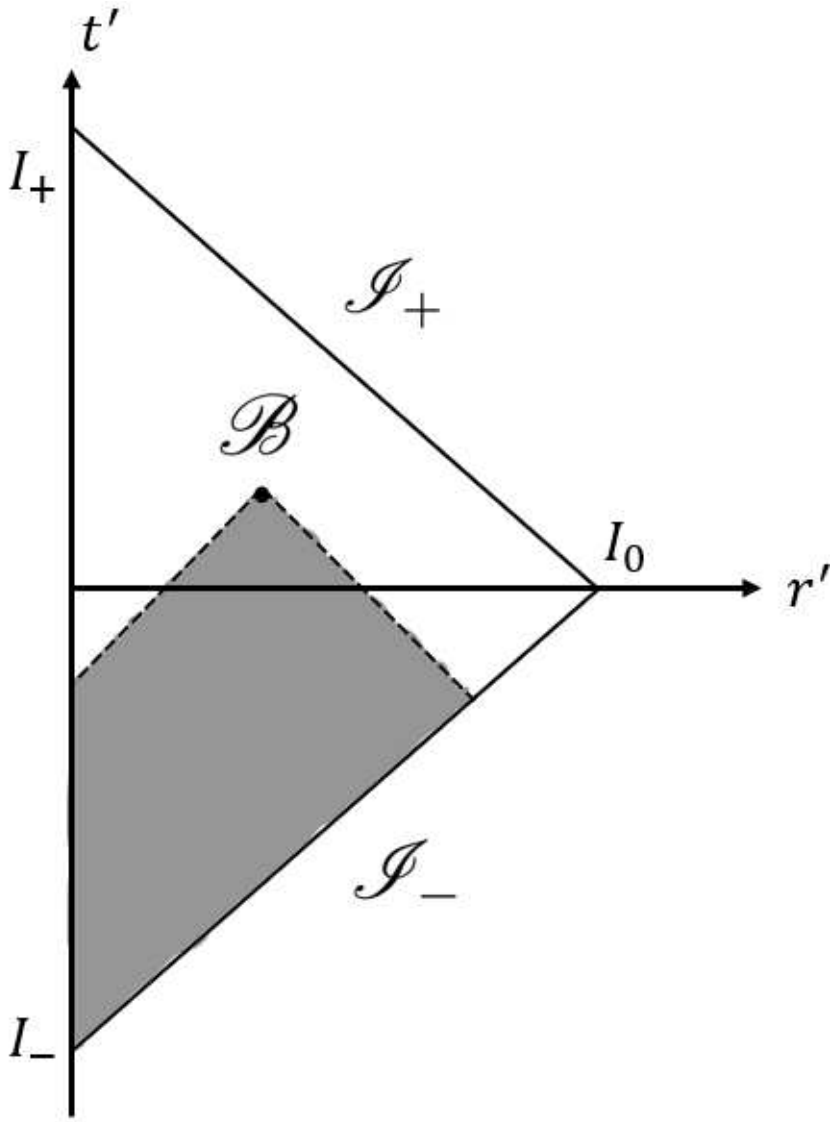

Figure 2.5: Penrose-Carter diagram for flat space with observer $\mathscr{B}$ shown at black dot. Shaded region denotes past light cone for observer.

from which $\mathscr{B}$ can receive information, this is known as the observer's past light cone.

2.5 Kruskal-Szekeres Coordinates

I shall now proceed to describing the main coordinates studied in this thesis, the maximal Schwarzschild extension, known as the Kruskal-Szekeres coordinates.

Consider the following transformations,

$$\begin{aligned} X_{r>2M} &= \left(\frac{r}{2M}-1\right)^{\frac{1}{2}} e^{\frac{r}{4M}} \cosh\left(\frac{t}{4M}\right) \\ T_{r>2M} &= \left(\frac{r}{2M}-1\right)^{\frac{1}{2}} e^{\frac{r}{4M}} \sinh\left(\frac{t}{4M}\right) \\ X_{r<2M} &= \left(1-\frac{r}{2M}\right)^{\frac{1}{2}} e^{\frac{r}{4M}} \sinh\left(\frac{t}{4M}\right) \\ T_{r<2M} &= \left(1-\frac{r}{2M}\right)^{\frac{1}{2}} e^{\frac{r}{4M}} \cosh\left(\frac{t}{4M}\right) \end{aligned} \tag{2.17}$$

Using the transformations (2.17) on the Schwarzschild metric (2.11) we find that in coordinates (T, X, θ, ϕ), the metric takes the form

$$ds^2 = \frac{32M^3}{r} e^{\frac{r}{2M}} (dX^2 - dT^2) + r^2(d\theta^2 + \sin^2\theta d\phi^2). \tag{2.18}$$

Here r is implicitly defined by the following equation,

$$\left(\frac{r}{2M}-1\right) e^{\frac{r}{2M}} = X^2 - T^2. \tag{2.19}$$

This form of the metric has some uniquely useful attributes that make it quite interesting to study. Specifically note that we no longer have a coordinate failure at the horizon. This means one can probe the interior of the black hole, but there is more to these coordinates. Considering the Schwarzschild Penrose-Carter diagram

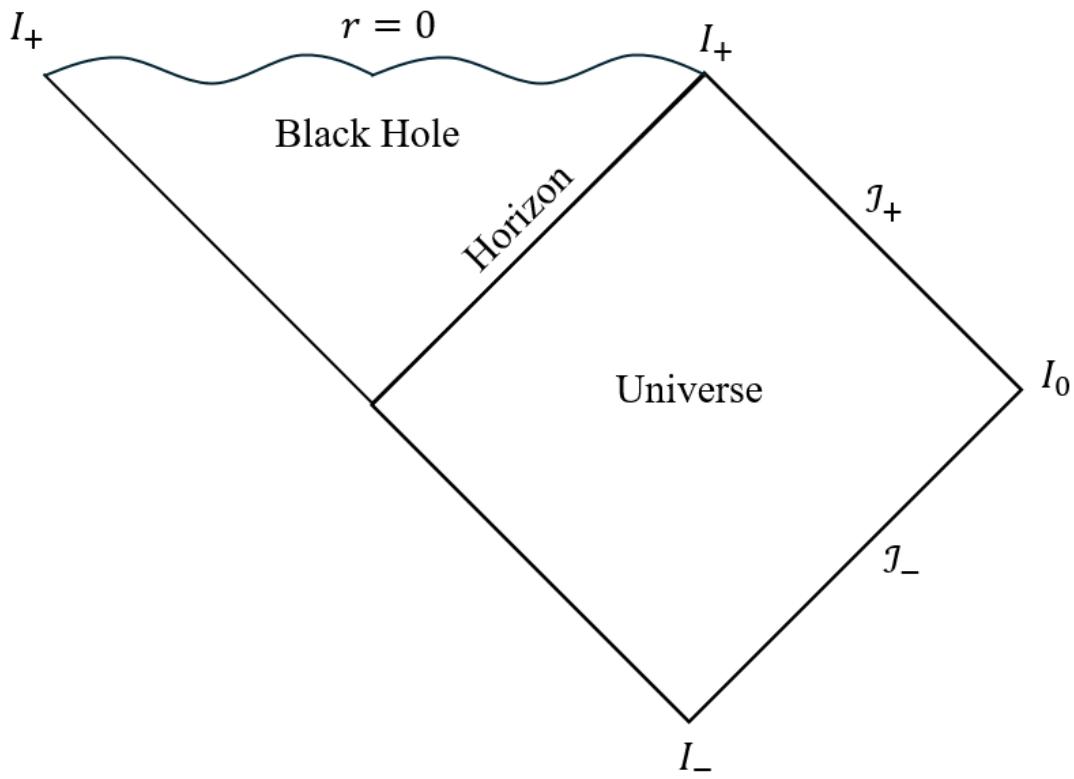

Figure 2.6: Partial Penrose-Carter diagram showing the black hole interior and exterior for the Schwarzschild solution. Note that here we use the same labelling methods as in 2.3.

depicted in Figure 2.6, along with the metric (2.11), there are two regions. The first region is our universe, while the second is the black hole. The labeling of Figure 2.6 follows the basic scheme described previously. If the Kruskal-Szekeres coordinates are shown in this manner, as in Figure 2.7, there are two asymptotically flat regions. One where $X \to \infty$ and another where $X \to -\infty$. One of the benefits of taking coordinates in this manner is that there is a way to examine slices of the spacetime without intersecting a singularity. This proves quite useful specifically in numerical relativity.

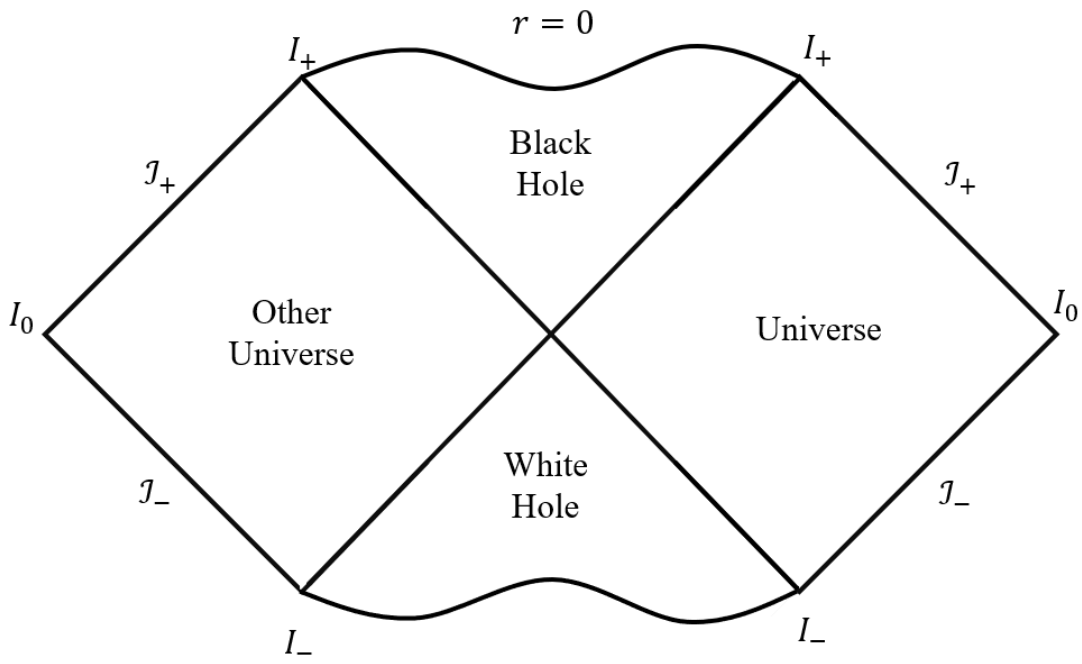

Figure 2.7: Full Penrose-Carter diagram for the Schwarzschild solution. This diagram is useful in the case of the Kruskal-Szekeres coordinates and shows two asymptotically flat regions, with a black hole and a white hole.

2.6 Marginally Outer Trapped Surfaces

The main focus of this thesis is *marginally outer trapped surfaces*, or MOTSs. To finalize this background information, I will define these surfaces. First consider some sphere S in Minkowski space. If light is emitted travelling both inwards and outwards from S, then a light-front sphere in the inward direction will always have S_1 smaller area than S, while S_2 in the outward direction will always have larger area than S.

However, if you consider this process for a surface of constant r, S inside a black hole, the strong gravitational field causes the light in both directions to fall inwards and both S_1 and S_2 will have their areas smaller than and enclosed by S. Such an S is called a *closed trapped surface*. Taking this a step further, if we find that the

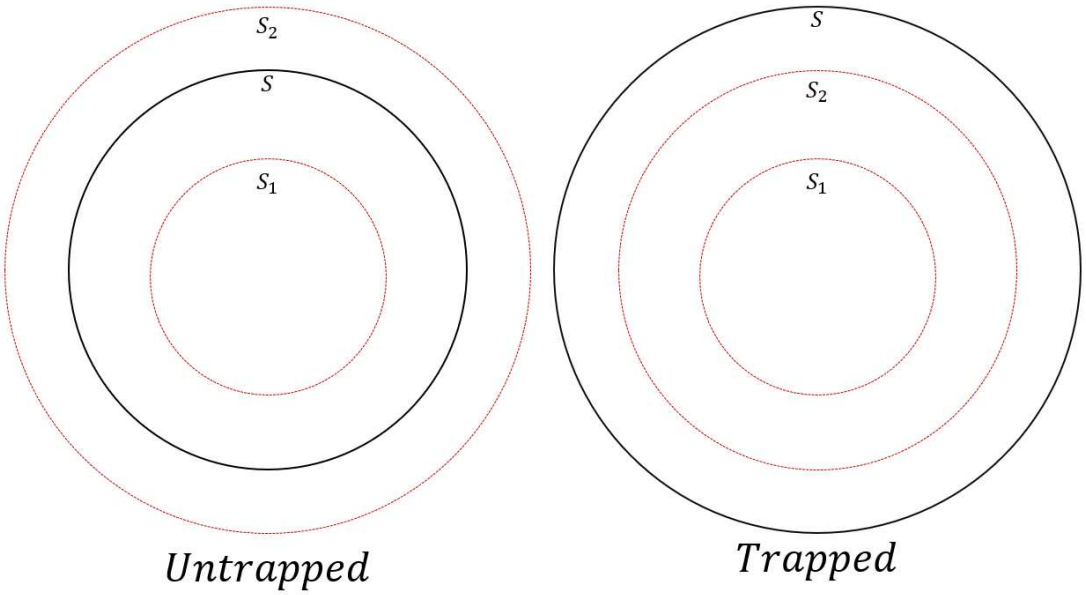

Figure 2.8: Diagram depicting trapped and untrapped surfaces by making use of a "sphere" S which emits light. This emission will result in outward and inward light that is depicted by the spheres S_1 and S_2.

outgoing light sphere S_2 has constant area (this light remains stationary) this means that the surface's *outgoing null expansion* is zero. We then refer to this surface as a *Marginally Outer Trapped Surface*.

We then wish to find equations for these MOTSs. We restrict our search to axisymmetric surfaces such that our equations describe curves within the (r, θ) plane (the "orbit" space) that can then be rotated into a full MOTS.

Consider that curves in two-dimensions can be written in the form

$$T^a \nabla_a T^b = \kappa N^b, \tag{2.20}$$

where T^a is the unit tangent, N^b is the unit normal, and κ is the acceleration. Thus, if we can find an expression for κ in the background geometry, we will have the required

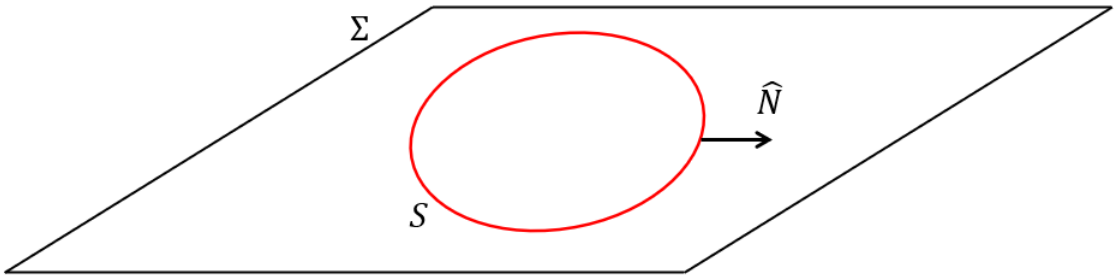

Figure 2.9: Diagram of some surface S living on some hypersurface Σ in some spacetime $\mathcal{M}$

"MOTSodesic" equations.

2.7 The MOTSodesic Equations

2.7.1 Overview of the MOTSodesic Equations

This section is an overview of results that we have used that were originally derived in [5]. For further details see that reference.

Begin by considering a surface S living on some hypersurface Σ within some spacetime with metric g_{ab}. This hypersurface has three-metric h_{ij} and extrinsic curvature K_{ij}. We restrict our attention to axisymmetric spacetimes and Σ and S with the same symmetry. Then if ϕ is the axial coordinate (2.21),

$$\frac{\partial}{\partial\phi}h_{ij} = \frac{\partial}{\partial\phi}K_{ij} = 0. \tag{2.21}$$

Following this, parameterize the surface S by (λ, ϕ) where λ is the arc length. This means we have unit tangent vectors,

$$\frac{\partial}{\partial \lambda} = \vec{T} \tag{2.22}$$

$$\hat{\phi} = \frac{1}{\left|\left|\frac{\partial}{\partial \phi}\right|\right|} \frac{\partial}{\partial \phi}. \tag{2.23}$$

To study the geometry of a surface S that lives in our hypersurface Σ, we pull back the three-metric h_{ij} to obtain the induced two-metric on S,

$$q_{AB} = e^i_A e^j_B h_{ij}. \tag{2.24}$$

In coordinate form, the pull-back operator takes the following form,

$$e^i_A = \frac{\partial x^i}{\partial \theta^A}. \tag{2.25}$$

Naively, but simply, these operators tell us how to write a vector on S as a vector in Σ by making use of the fact that if you can make measurements in the spacetime the surface lives in, you can make measurements within the surface. Then

$$q_{AB} u^A v^B = (h_{ij} e^i_A e^j_B) u^A v^B = h_{ij} (e^i_A v^A)(e^j_B v^B) = h_{ij} u^i v^j. \tag{2.26}$$

To understand how the pull-back operators work consider that if there is some metric h_{ij}, then this describes how to make measurements in said spacetime. We can equivalently take the dot product of two vectors u^A and v^B in the surface with respect to the pull-back metric q_{AB} or the product of their push-forwards u^i and v^j with respect to h_{ij}.

One can write the induced two-metric on the surface in an orthonormal basis,

$$q_{AB} = T_A T_B + \hat{\phi}_A \hat{\phi}_B. \tag{2.27}$$

The trace of the extrinsic curvature of S in Σ is defined by the following,

$$k_N = q^{ij} D_i N_j, \tag{2.28}$$

where N here is the normal to S, which is unit length. It is obtained by finding the outward-oriented unit vector that is perpendicular to the push-forward of T and $\hat{\phi}$. D is the h_{ij} compatible covariant derivative. Then using (2.28) and (2.27), the following form for the extrinsic curvature on S in this axisymmetric slice can be constructed,

$$k_N = (T^i T^j + \hat{\phi}^i \hat{\phi}^j) D_i N_j \tag{2.29}$$

$$= -N_j T^i D_i T^j + \hat{\phi}^i \hat{\phi}^j D_i N_j \tag{2.30}$$

$$= -\kappa + \hat{\phi}^i \hat{\phi}^j D_i N_j, \tag{2.31}$$

where $\kappa = N_j T^i D_i T^j$. Alternatively, given k_N we can write

$$\kappa = -k_N + \hat{\phi}^i \hat{\phi}^j D_i N_j. \tag{2.32}$$

Following this work, consider that, as stated previously in the introduction of this thesis, a MOTS is a surface in some Σ with a vanishing outward null expansion. If $\hat{u}$ is the forward-in-time pointing timelike normal to Σ, then the outward null normal is $\ell = \hat{u} + \hat{N}$ and the associated expansion is

$$\theta_\ell = q^{ab} \nabla_a \ell_b = q^{ab} \nabla_a \hat{u}_b + q^{ab} \nabla_a \hat{N}_b = q^{ij} K_{ij} + k_N. \tag{2.33}$$

Then if $\theta_\ell = 0$, $\kappa = -q^{ij}K_{ij}$ and so by (2.32),

$$\kappa = q^{ij}K_{ij} + \hat{\phi}^i\hat{\phi}^j D_i N_j. \tag{2.34}$$

Next, consider $(P(\lambda), \Theta(\lambda))$ as a curve in the (r, θ) plane. Then as for any two-dimensional curve we can write

$$T^A \nabla_A T^B = \kappa N^B, \tag{2.35}$$

where κ is now understood as the curvature of $(P(\lambda), \Theta(\lambda))$ in the plane.

Through some final works of applying the equations defined in this section, a final general set of equations for finding these surfaces of interest is constructed,

$$\dot{T}^k = -\Gamma^k_{ij} T^i T^j + \kappa N^k, \tag{2.36}$$

where κ is calculated from (2.34), Γ^k_{ij} are the Christoffel symbols for h_{ij} in Σ, and the overdot is a derivative with respect to λ.

Thus, if the extrinsic curvature K_{ij} and three-metric h_{ij} of Σ are known, we can solve (2.36) to find axisymmetric MOTSs. This process also involves calculating the Christoffel symbols Γ^k_{ij}, coordinate representations of the unit vectors N, $\hat{\phi}$, and T, then finally solving (2.36). All of this was done through Mathematica, with the final second order equations by using Mathematica's NDSolve package. This can be done as long as there are initial values for location and direction (T). Note here though that we must use an expansion for some of the initial conditions, as their definitions diverge at the values you wish to initialize at in some instances.

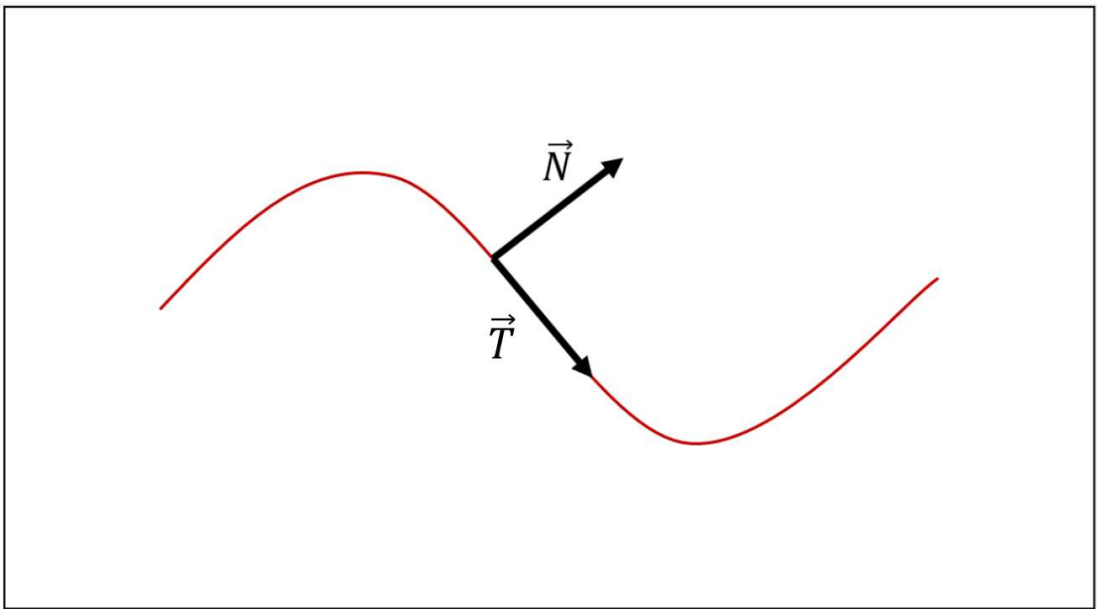

Figure 2.10: Diagram depicting perpendicular nature of $\vec{T}$ and $\vec{N}$ on a curve within a plane.

2.7.2 MOTSodesic Equations in Kruskal Slices

Since the general solving method has now been described, I shall finish this section with a derivation of the coordinate versions of the Kruskal-Szekeres MOTS equations using the systematic formalism developed in [15]. For a $T =$ constant surface, (2.18) implies that

$$h_{ij}dx^i dx^j = \alpha^2 dX^2 + r^2 d\Omega^2, \tag{2.37}$$

while the extrinsic curvature for this surface is

$$K_{ij}dx^i dx^j = \alpha_T dX^2 + \frac{rr_T}{\alpha}d\Omega^2. \tag{2.38}$$

Note that in the definitions (2.37) and (2.38) we have a new function α. This has the following definition,

$$\alpha^2 := \frac{32M^3 e^{\frac{-r}{2M}}}{r}. \tag{2.39}$$

As discussed in the previous section we only study axisymmetric surfaces. Then we define the orbit space as any $\phi =$ constant hypersurface $\overline{\Sigma}$ with induced two-metric $\underline{h}_{ab}$. This is the (X, θ) half plane. Thus, the two-metric can be written in the following manner,

$$\underline{h}_{ab} dx^a dx^b = \alpha^2 dX^2 + r^2 d\theta^2. \tag{2.40}$$

The next step in finding the MOTSodesic equations is to calculate the Christoffel symbols Γ,

$$\begin{aligned} \underline{\Gamma}^X_{XX} &= \frac{\alpha_X}{\alpha} \\ \underline{\Gamma}^X_{\theta\theta} &= -\frac{r r_X}{\alpha^2} \\ \underline{\Gamma}^\theta_{X\theta} &= -\frac{r_X}{r}. \end{aligned} \tag{2.41}$$

The tangent and normal vectors $\hat{T}$ and $\hat{N}$ in our Kruskal-Szekeres coordinates are

$$\hat{T} = \dot{P}\frac{\partial}{\partial X} + \dot{\Theta}\frac{\partial}{\partial \theta}, \tag{2.42}$$

$$\hat{N} = \frac{r}{\alpha}\dot{\Theta}\frac{\partial}{\partial X} - \left(\frac{\alpha}{r}\right)\dot{P}\frac{\partial}{\partial \theta}. \tag{2.43}$$

Note that a hat is used in (2.42) and (2.43) due to these vectors being of unit length. In the paper [5], κ is shown to be

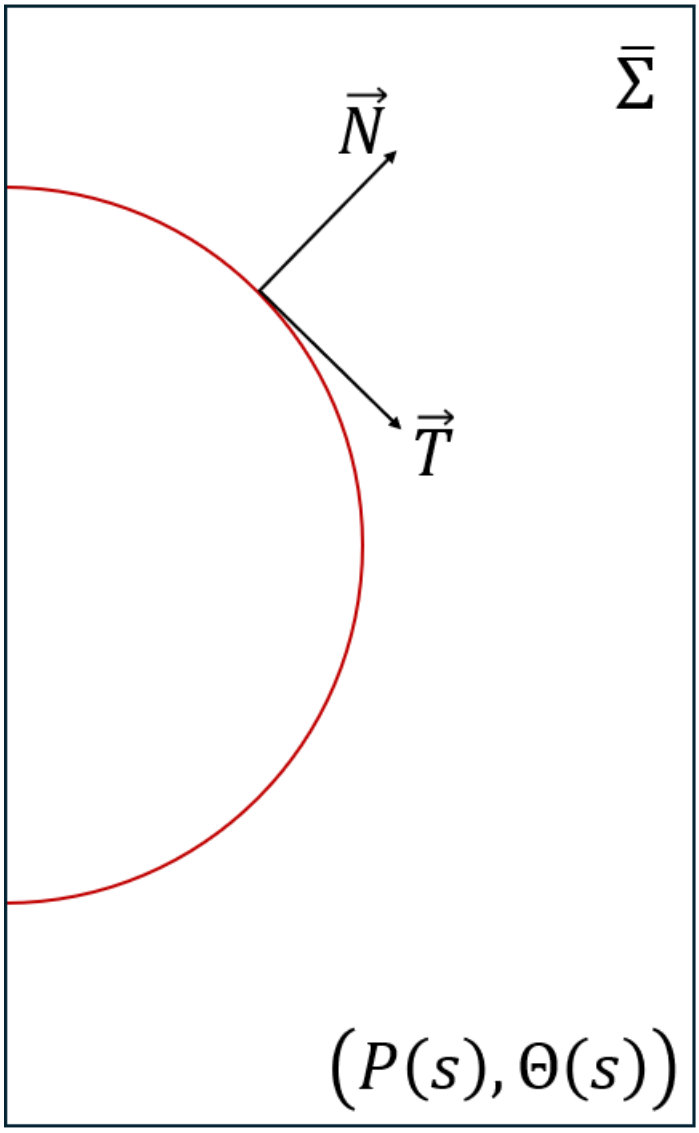

Figure 2.11: Diagram of orbit space $\bar{\Sigma}$ with some curve living on the space with tangent vectors $\vec{N}$ and $\vec{T}$.

$$\kappa = \mathcal{K} + \mathcal{K}_{\hat{N}} + \mathcal{K}_{\hat{T}\hat{T}}, \tag{2.44}$$

where the definitions for each of the $\mathcal{K}$ terms are as follows [15],

$$\begin{aligned}
\mathcal{K} &:= h^{\phi\phi} K_{\phi\phi} \\
\mathcal{K}_{\hat{N}} &:= \hat{N}^a \underline{\nabla}_a (\ln \sqrt{h_{\phi\phi}}) \\
\mathcal{K}_{\hat{T}\hat{T}} &:= K_{ij} \hat{T}^i \hat{T}^j.
\end{aligned} \tag{2.45}$$

Making use of the definitions (2.37), (2.38), (2.43), and (2.42), we calculate these terms for our Kruskal-Szekeres spacetime as:

$$\begin{aligned}
\mathcal{K} &= \frac{r_T}{\alpha_r} \\
\mathcal{K}_{\hat{N}} &= \dot{\Theta} \frac{r_X}{\alpha} - \frac{\alpha \cot \Theta \dot{P}}{r} \\
\mathcal{K}_{\hat{T}\hat{T}} &= \alpha_T \dot{P}^2 + \frac{r r_T}{\alpha} \dot{\Theta}^2.
\end{aligned} \tag{2.46}$$

Then, finally, after all of the equation work is done, combine these pieces along with the general derivation scheme described previously to obtain the equations for finding MOTSs in the Kruskal-Szekeres spacetime,

$$\begin{aligned}
\ddot{P} &= -\left(\frac{\alpha_X}{\alpha}\right) \dot{P}^2 + \left(\frac{r r_X}{\alpha^2} \dot{\Theta}^2\right) + \left(\frac{r\kappa}{\alpha}\right) \dot{\Theta} \\
\ddot{\Theta} &= -\left(\frac{2 r_X}{r}\right) \dot{P} \dot{\Theta} - \left(\frac{\alpha \kappa}{r}\right) \dot{P}.
\end{aligned} \tag{2.47}$$

The required equations have now been derived, and the means in which they will be solved has been discussed. From here, the natural progression is to discuss how efficient our numerical methods are at solving these equations. Thus, in the next section of this thesis I will analyze the stability and uncertainties in the solvers utilized in this research.

2.8 Uncertainty in Numerics

After the equations have been derived as described in the previous Section 2.7, the pair of coupled ordinary differential equations (2.47) are obtained which are solved using Mathematica's NDSolve. Before any assertions on the properties of solutions are made, there must be some discussion about the uncertainty involved. I note here that uncertainty analysis is difficult in this case because most of these solutions have no analytical counterpart and a shooting method is being utilized. This means that one cannot directly calculate a measurement of how far away they are from some "correct" solution because we have no such analytic solution.

Even though it is true that there are no analytical solutions for most MOTSs, that of the outer horizon is known. Using this information, the first analysis that could be done was to compare NDSolve's solution of the MOTS equations at the outer horizon location to the known analytical result. Doing this should provide some idea of the uncertainties involved with our solution. It is noted that there are some components of our solver that will cause some inherent uncertainty. First, the boundary conditions can not be exact. As stated in Section 2.7 it is seen that, for example, the initial θ value has to be approximately zero but can not be exactly zero or there will be errors in the equations. There are some remedies to this issue however. One option is doing a series expansion of the solution near $\theta = 0$ to provide an expression for our initial conditions. This was done before with a third order Taylor expansion [15], which would result in a third order uncertainty in our solution. Accounting for this inherent error, I then do a simple difference of the analytical solution to the solver's solution at the horizon. The solution, along with the results shown in this thesis, used NDSolve with an explicit sixth order Runge-Kutta scheme, with a fixed step size of $h = 0.00001$, while the grid runs from zero to π.

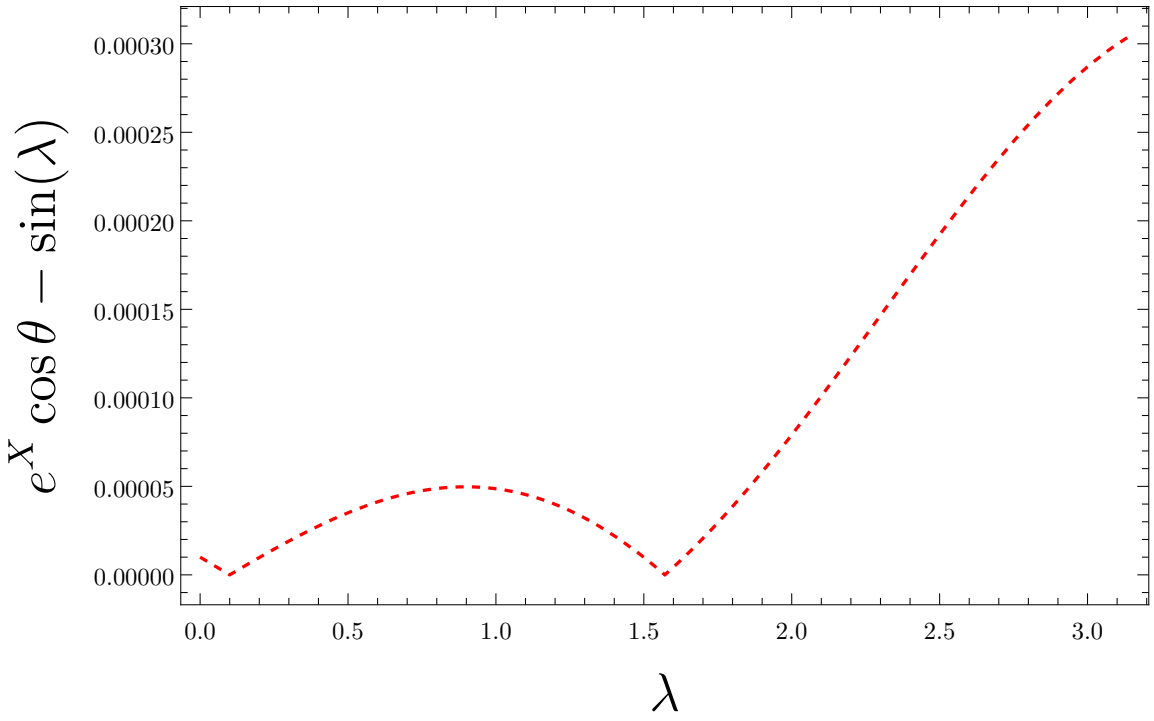

Figure 2.12: Absolute error in solution of outer horizon MOTS. Plot is created by differencing NDSolve's solution for a surface at the outer horizon location and the known analytical solution at that point.

It is shown in Figure 2.12 that there exists some error in our solution, but within acceptable magnitudes. This is the simplest case however, so there must be further work done to determine the convergence of our solutions that have no analytical counterpart. To determine such things, I first consider that one can write numerical solutions as expansions. Say we have some solution s with grid spacing h. We can write this in an expanded form

$$s(h) = s^* + h^p e_p + h^{p+1} e_{p+1} + ... \tag{2.48}$$

Note here that e is some error term in (2.48). If we then assume that h is always

sufficiently small, the following relation can be written,

$$s(h_1) - s(h_2) \approx (h_1^p - h_2^p)e_p. \tag{2.49}$$

Thus, with some algebraic work, one may find the following relation that allows for estimating the rate of convergence p,

$$\frac{||s(h_2) - s(h_3)||}{||s(h_1) - s(h_2)||} = r^p, \tag{2.50}$$

where r is initial grid spacing which is $r = \frac{1}{10}$ in this case. Thus, taking a log with base 10 on both sides results in the following,

$$\log_{10} \frac{||s(h_2) - s(h_3)||}{||s(h_1) - s(h_2)||} = -p. \tag{2.51}$$

I then move to solving for the one-looping MOTS at the $T = 0.5$ slice while using the same solver as before, NDSolve with an explicit sixth order Runge-Kutta method (like shown in the left-most plot in Figure 2.13). Considering (2.51), we must start with three different grid sizes, all with the relation $h_{i+1} = rh_i$. Meaning while $h_1 = \frac{1}{10}$, the next will be $h_2 = \frac{1}{100}$ and $h_3 = \frac{1}{1000}$. This is then done for three different cases, such that the initial h value decreases in size by r each time, resulting in a graph that gives some insight as to the convergence of our solutions.

From Figure 2.14 we see a convergence rate of $p \approx 2.5$ which is acceptable for this research. As stated before, we expect a sixth order uncertainty from our Runge-Kutta method, as well as a third order uncertainty from our expansion of some of the initial conditions of the solution. This is to say that the convergence rate found sounds no alarms, allowing us to move on to the broader scope of the research while using the methods I have tested.

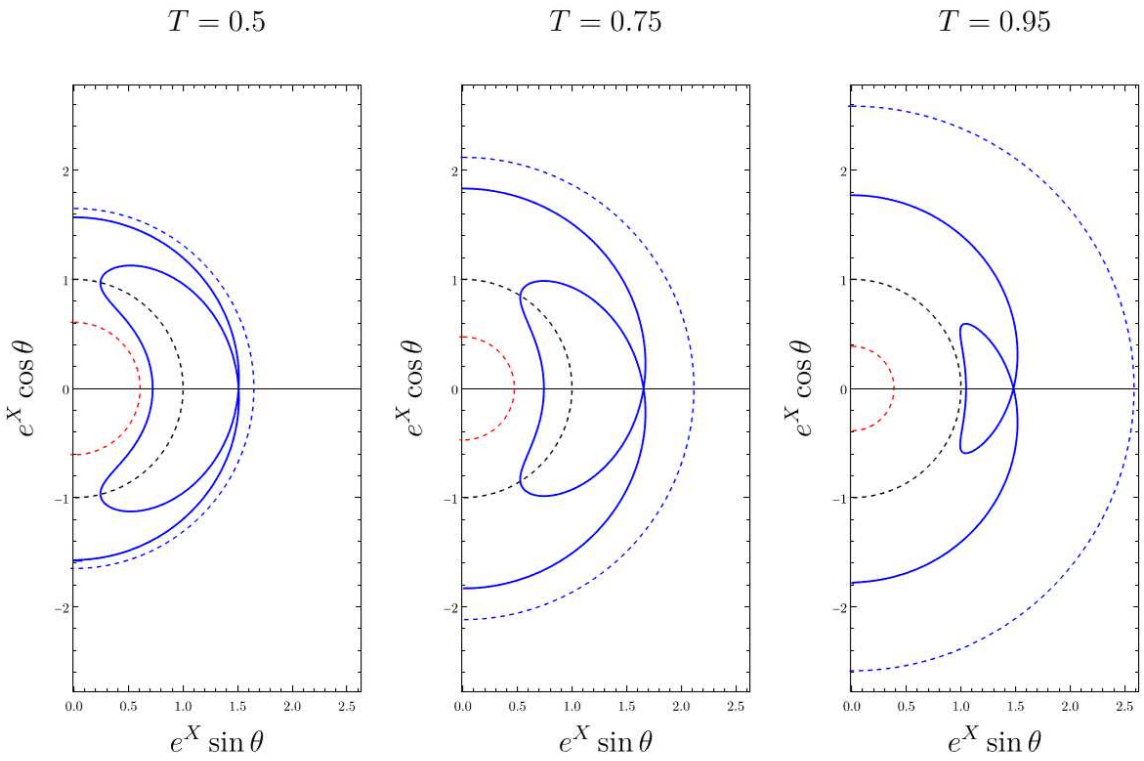

Figure 2.13: The one-looping MOTS tracked from the $T = 0.5$ slice to the $T = 0.95$ slices. The dashed blue line is our universe's black hole horizon, the solid blue line is the MOTS, the dashed black line is the "throat", and the dashed red line is the other universe's black hole horizon. Note the receding nature of the inner portion of the loop as T increases.

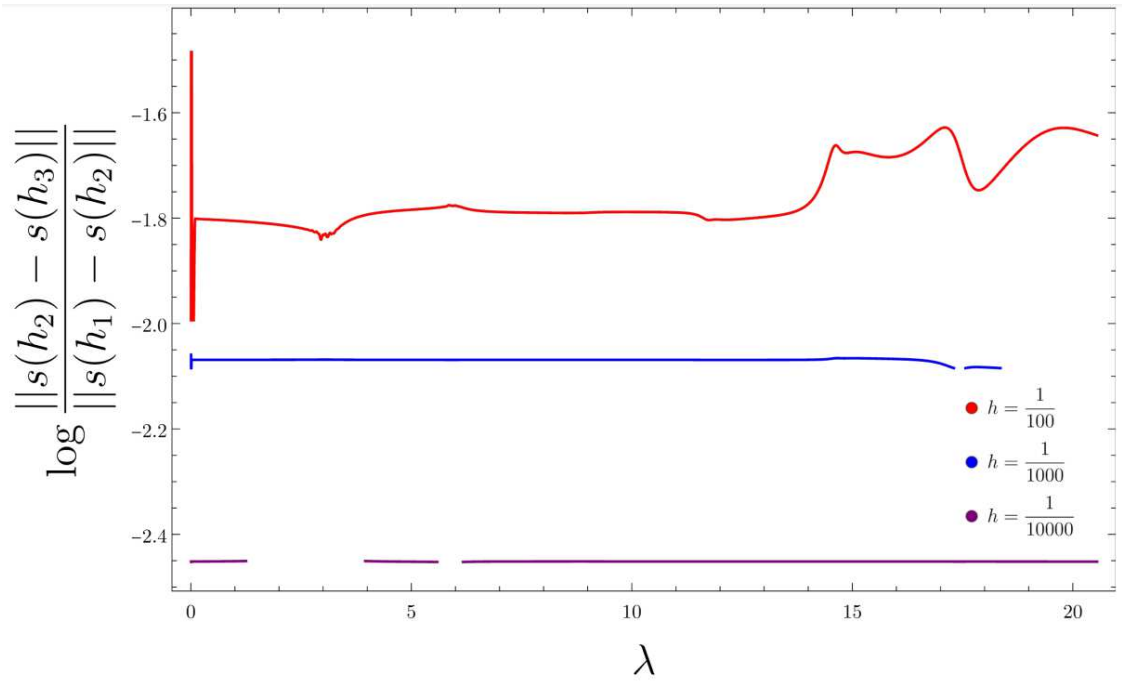

Figure 2.14: Convergence factor p for the one-looping MOTS at $T = 0.5$, which is shown as the leftmost plot of Figure 3.5. Found through using (2.51) while the h in the legend shows different values of h_1 for the solutions, such that h_2 and h_3 are determined by $h_{i+1} = rh_i$, where $h = r = h_1$ for each curve in the plot. Plot shows convergence of approximately 2.5 which is acceptable for the purposes of this research.

Chapter 3

Exploration of Marginally Outer Trapped Surfaces

3.1 Plotting Methods for MOTS

In Section 2.8 a method for solving the MOTS equations was been constructed. Representing these solutions in plots is not completely trivial and so we now discuss how this is done. Consider first that the equations that have been constructed are two-dimensional cross-section curves representing axisymmetric surfaces in our space $\mathcal{M}$ in some hypersurface Σ. It is always important to visualize results in the cleanest way possible, such that anyone examining these visualizations can best understand and appreciate the results found. There are two plotting methods used for the majority of the results found in this thesis work, along with accompanying works [15]: 1) that of the polar-like two-dimensional curve plots and 2) the embedding methods. There is also a third plotting method that has been used for some high T MOTSs in the Kruskal-Szekeres work. This method is method (1) with a coordinate transformation such that the results resemble results from works studying other spacetimes, specif-

ically surfaces found in Eddington-Finkelstein-like coordinates. Let us first describe and examine the first of the two plotting methods.

The polar-like plotting method is a simple map such that properties in our infinite spacetime are shown in a compact way. The mapping is

$$(x, y) = (e^X \cos(\theta), e^X \sin(\theta)). \tag{3.1}$$

Let us then describe some of the important features of this representation. At the origin of our plots, $(0, 0)$, the X coordinate approaches negative infinity. Meanwhile as $X \to \infty$, $(x, y) \to (\infty, \infty)$. Compare this with the Penrose-Carter diagram for the Kruskal-Szekeres spacetime shown in Figure 3.1. At the right-most corner of that diagram, there is positive spacelike infinity, which is covered by our slice, as well as the left-most point, which is $X = \infty$, the infinity in the other universe. Then if you are far away from the origin in our described plotting method, you would then be approaching the right-most portion of the slice on the Penrose-Carter diagram. Conversely, if we approach the origin in our plot, we approach the left-most point in our slice on the Penrose-Carter diagram, meaning we go to infinity in the other universe. This method provides quite a useful visualization of the surfaces we consider, so, this is the main method of plotting used in this work, along with many other MOTS finding works.

Now that I have described the main plotting method for this work, let us walk through the process of finding and visualizing a MOTS. Once initial conditions are determined, a shooting method is utilized and the user must sift through initial values of X until a closed surface is found at some slice T. There is some nuance to using this method but it has become a comfortable method to use for a fine-tuned search.

The process of finding the MOTSs in some slice of constant T begins from the known outer-most MOTS in the slice, the outer horizon at $X = T$. From here, begin

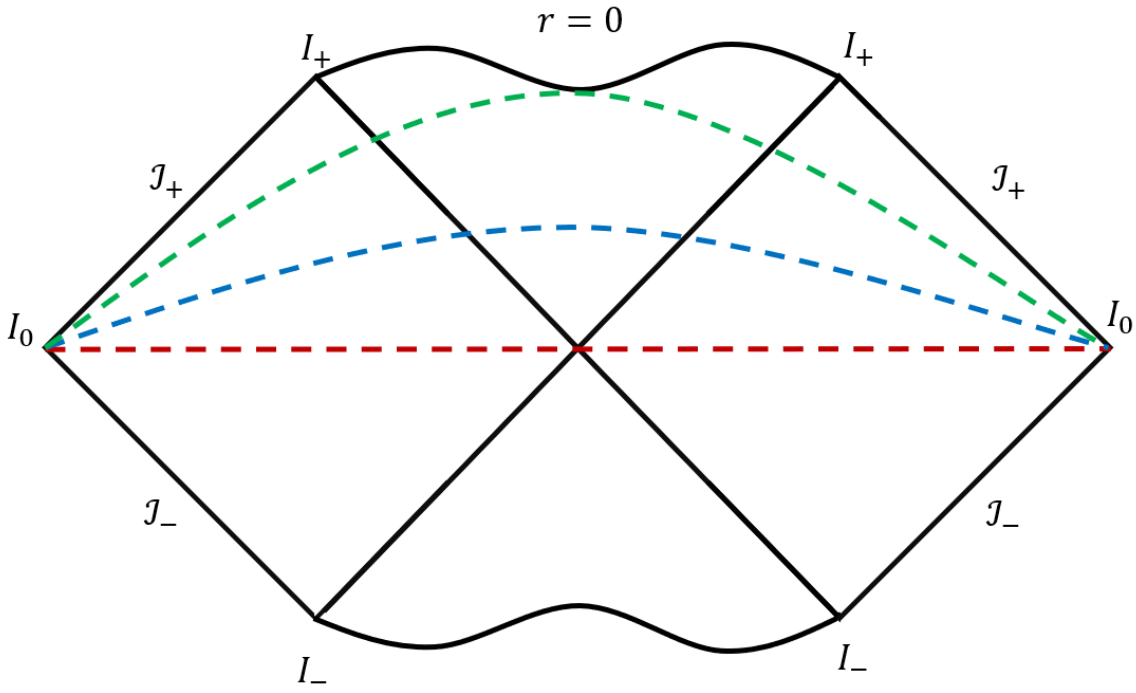

Figure 3.1: Penrose-Carter diagram for the Kruskal-Szekeres Schwarzschild coordinates. The red line here is the $T = 0$ slice, the blue line would be approximately the $T = 0.5$ slice, and the green line is the $T = 1$ slice.

shooting from incrementally smaller values of X until a closed surface is found. This can be done by recognizing a key feature in the MOTS finding process that begins with noticing a outward curl, then an inward curl, and the realization that between these points there must be closure, which is just a 90 degree touchdown at the vertical axis. This process is depicted in Figure 3.2. Remember that closure is required and it is shown in this manner due to the MOTS being a closed surface with axisymmetry we have defined in Section 1.1.

Throughout, this plotting method will be the one most used. However, there is also a nice way to visualize the surfaces found in a "three dimensional" manner called the embedding diagram. I will now move to a discussion of those diagrams.

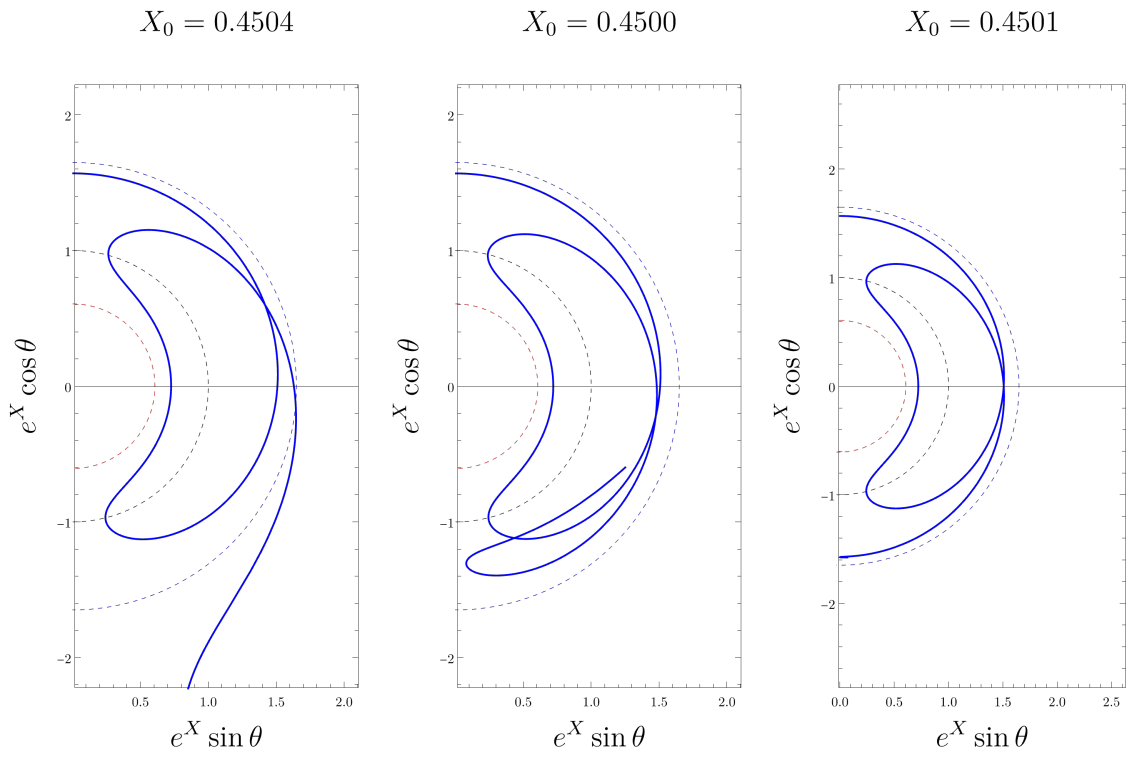

Figure 3.2: Collection of plots showing the progression of the shooting method as would be used by a user trying to search for a MOTS. Starting from the outer horizon at $X = T$, decrease X until a looping surface with an open outward curl is found (left-most plot). Then after finding an inward curl nearby (middle plot), there must be a point of closure between the two initial X values (right-most plot).

The goal of embedding diagrams is to visualize the connection between slice behaviours and the MOTS on the slice. I shall now describe how this is done in the specific case of this thesis work, along with reference [15]. Consider the cylindrical coordinates (ρ, z, ϑ). We wish to find a cylindrical surface parameterized by $z = z(X)$ and $\rho = \rho(X)$, which has induced metric

$$ds^2 = \left(\frac{dz^2}{dX^2} + \frac{d\rho^2}{dX^2}\right) dX^2 + \rho^2 d\vartheta^2. \tag{3.2}$$

Note that one can find (3.2) by simply plugging $z = z(X)$ and $\rho = \rho(X)$ into the general metric for cylindrical coordinates. Using both the new definition (3.2) along with the definition of the orbit space metric (2.40) we find the embedding equations are the following:

$$\begin{aligned} \theta &= \vartheta \\ \rho &= r(X) \\ \frac{32M^3 e^{\frac{-r}{2M}}}{r} &= \left(\frac{dz^2}{dX^2} + \frac{d\rho^2}{dX^2}\right). \end{aligned} \tag{3.3}$$

By solving these equations (3.3) we can generate plots of MOTSs on slices Σ which depict how the MOTSs looks in relation to these slices.

Note that in Figure 3.3 we are plotting from the equations (3.3). So, the diagram may appear to be just half of what one might think it should be. However, this is not the case, as we are plotting θ all the way from zero to π. However, it can be useful, or perhaps visually stimulating, to mirror the diagram such that a prettier diagram is achieved. This is then a cross-section covering both $\phi = 0$ and $\phi = \pi$.

With this mirroring, the behaviour of the MOTS in relation to the wormhole can be depicted in a slightly more intuitive manner.

As stated previously, the curve plotting method will be the main method of plotting in this thesis work. However, when embedding diagrams could aid in illustrating the relation between a particular MOTS and the slice it lives on, I shall also make use of these diagrams.

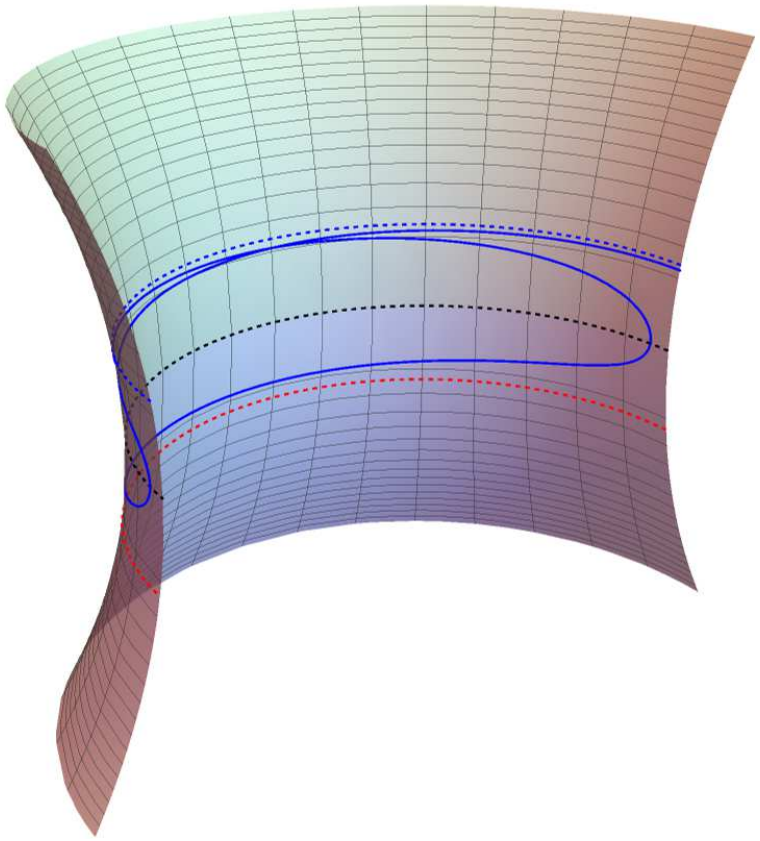

Figure 3.3: Embedding diagram for the one-looping MOTS at $T = 0.25$. The familiar plotting scheme is applied, with the dashed blue line representing the outer horizon of the black hole in region one, the dashed red line representing the outer horizon of the black hole in region two, the dashed black line representing the throat of the wormhole, and finally, the solid blue line being the MOTS.

3.2 N-looping MOTSs

Utilizing the solver described in Section 2.8 along with the plotting methods from Section 3.1, the process of depicting the results found during this research begins. In this section, only self-intersecting MOTSs are considered. These surfaces, as mentioned in Section 1.1, are similar to surfaces found when searching for MOTSs in other

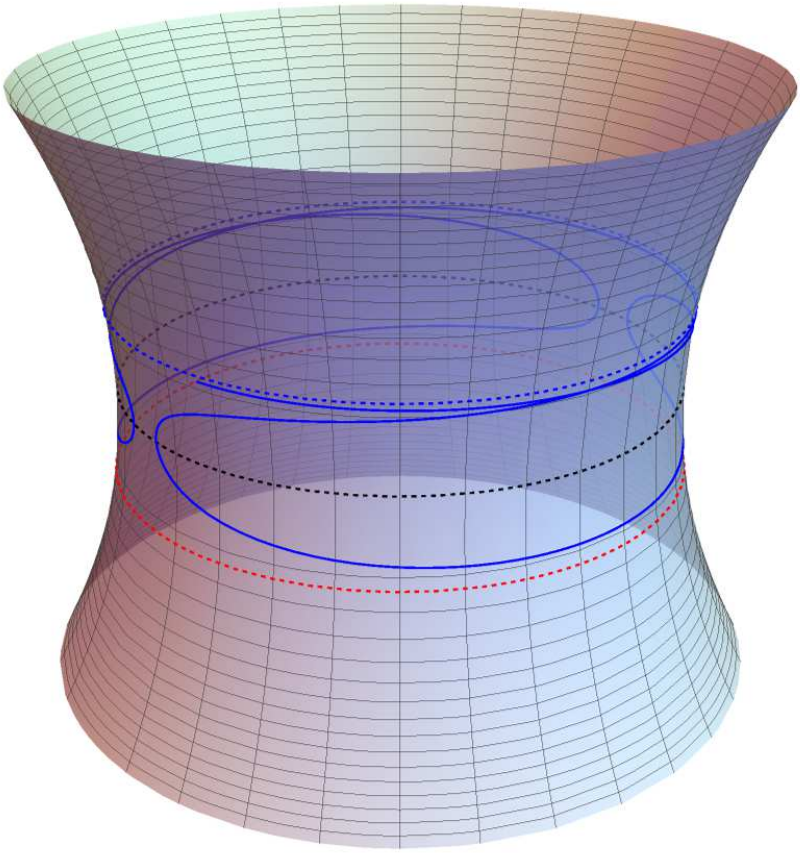

Figure 3.4: Embedding diagram constructed by mirroring Figure 3.3. This diagram now covers the domain $\theta \in (0, 2\pi)$, but only in the sense that we have mirrored the previous domain of $\theta \in (0, \pi)$.

spacetimes such as Reissner-Nordström, Schwarzschild Painlevé-Gullstrand, and more [11].

The first result concerns the MOTS with N-loops for which, as for other spacetimes [11], there appear to be an infinite number [4]. In the original papers which studied these surfaces in the Painlevé-Gullstrand coordinates, it was found that there were a potentially infinite number of these surfaces on any time slice τ (Figure 1.3). Here, in the Kruskal-Szekeres coordinates, we find that this appears to be the case as well.

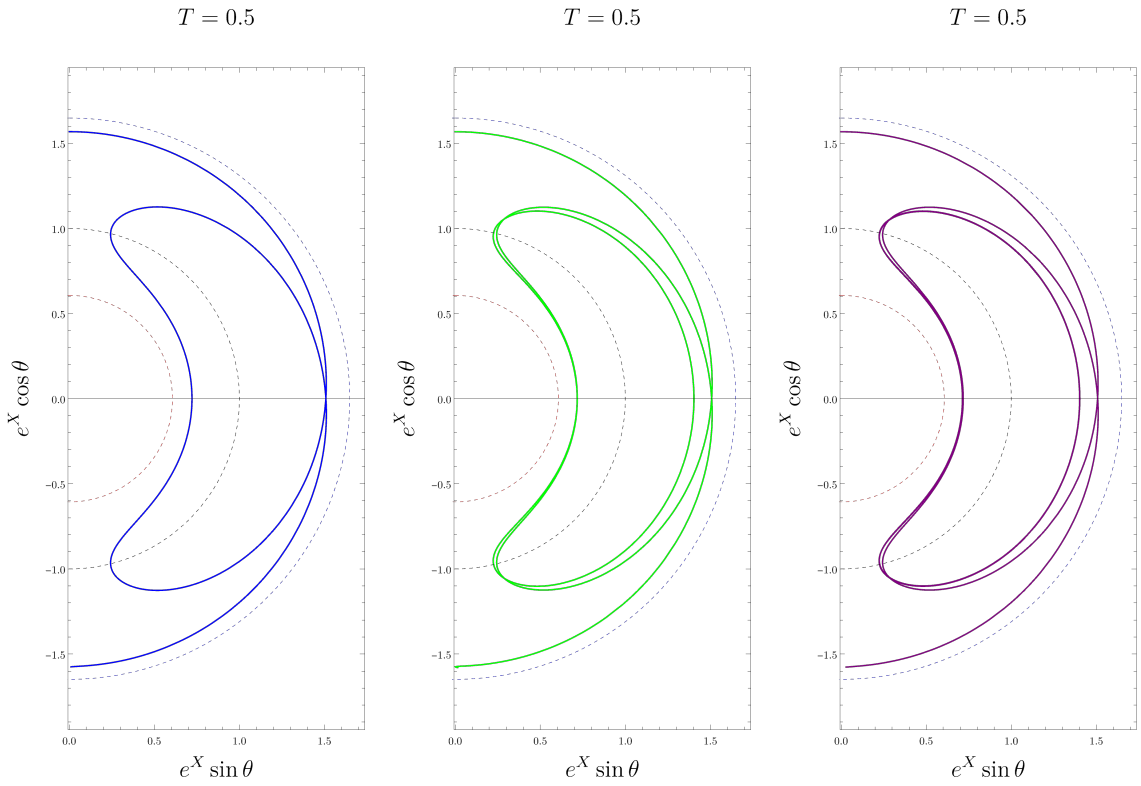

Figure 3.5: The one-, two-, and three-looping MOTS plotted from left to right to illustrate the many surface existence at some time slice T. The outer dashed blue line is the outer horizon of the black hole. The solid blue, green, and purple lines, are the N-looping MOTSs. While the black and red dashed lines are the throat and other universe's black hole horizon respectively. The two- and three-looping surfaces look nearly identical, which is due to the second and subsequent loops being essentially perturbations of the toroidal part of the MOTS.

Shown in Figure 3.5 are the one, two, and three looping examples. Further loops can be found but are not shown here. A convergence analysis is done for the leftmost MOTSs shown in Figure 3.5 in Section 2.8, which can be seen in Figure 2.14.

Another type of self-intersecting surface that is found begins in the positive ($0 <$

$\theta < \frac{\pi}{2}$) $e^X \cos\theta$ portion of the graph, and returns to the same positive $e^X \cos\theta$ portion, as opposed to the ordinary behaviour of moving from the positive portion to the negative ($\frac{\pi}{2} < \theta < \pi$), as in Figure 3.6. A key observation to note is that these surfaces are also topologically spherical, like the other surfaces shown in this section. This is an important observation because one of the main focuses of this work, the toroidal MOTSs, are in fact not topologically spherical. Pointing out that all of the N-looping surfaces are topologically spherical makes the toroidal surfaces feel that much more exotic. I will also describe how these surfaces behave at the extremities of slice values. These values would be when $T \to 1$ and $T \to 0$.

3.3 Behaviour as $T \to 1$

Considering Figure 2.7, what does our slicing of the spacetime look like?

From Figure 3.1 it can be seen that if you increase T, the slice reaches closer towards the black hole singularity. At slices $T > 1$, the singularity will be included in the slice. This means that if we consider the initial conditions described in Section 1.1, only MOTSs residing within our universe's black hole will be found, as the slice has been "split" into two pieces by the singularity.

In Figure 2.13, the consistent plotting method is applied. Let us consider the leftmost plot and describe its behaviour. Beginning with initializing on the positive y-axis, the MOTS's loop dips past the throat and into the other universe's black hole, before returning to our universe's black hole and then closing on the negative y-axis. Now consider the rightmost plot. Notice that the inner portion of the loop does not dip into the other universe anymore. This leads to the conjecture that as $T \to 1$, MOTSs, whose north and south poles are within our universe, pull back completely into our universe. This is consistent with our understanding of Figure 3.1 because

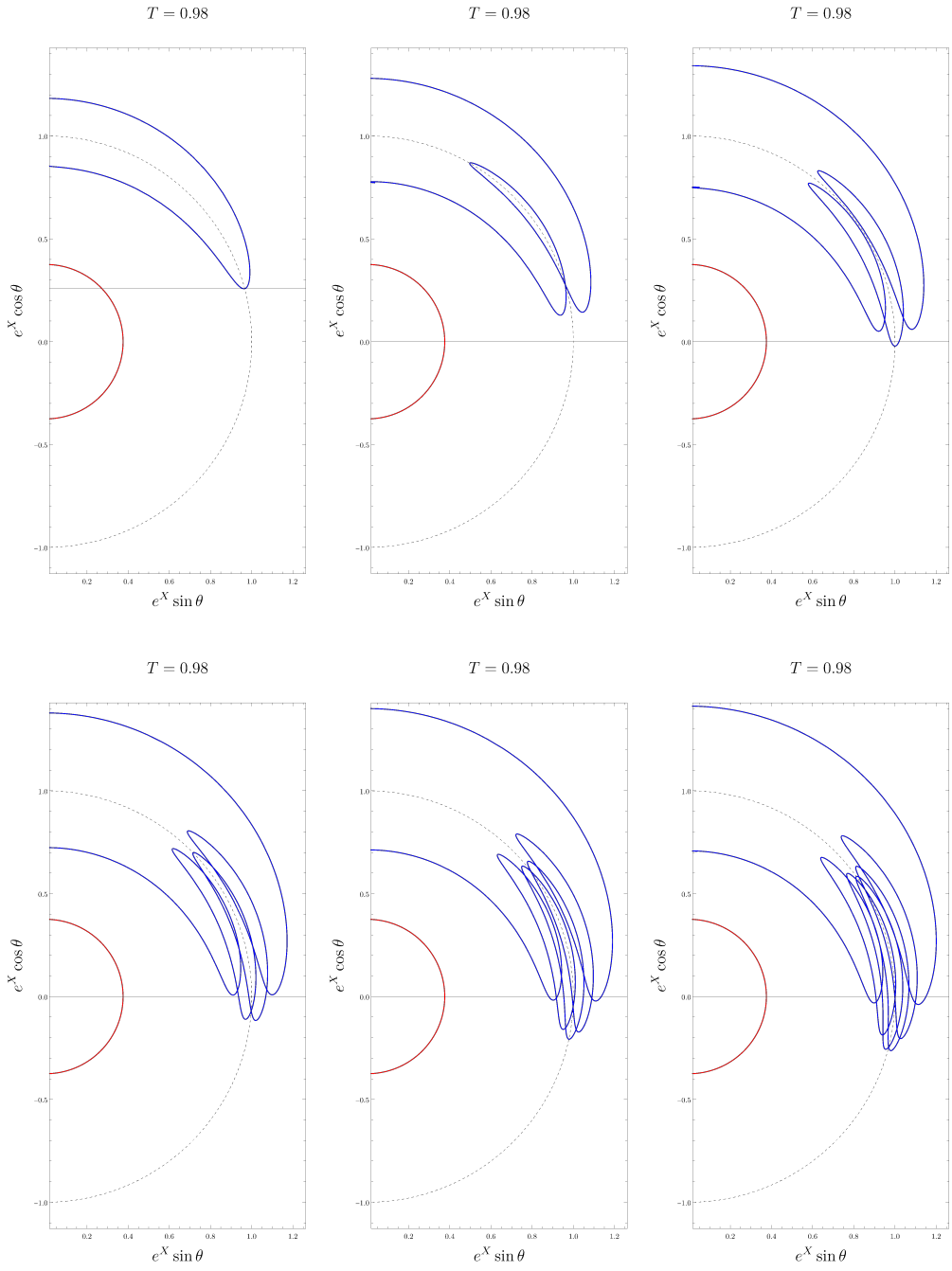

Figure 3.6: Launching from different initial values to find MOTSs that return above the horizontal axis. We see N-looping returning above MOTSs. N increases as you proceed from top left to bottom right in the plots.

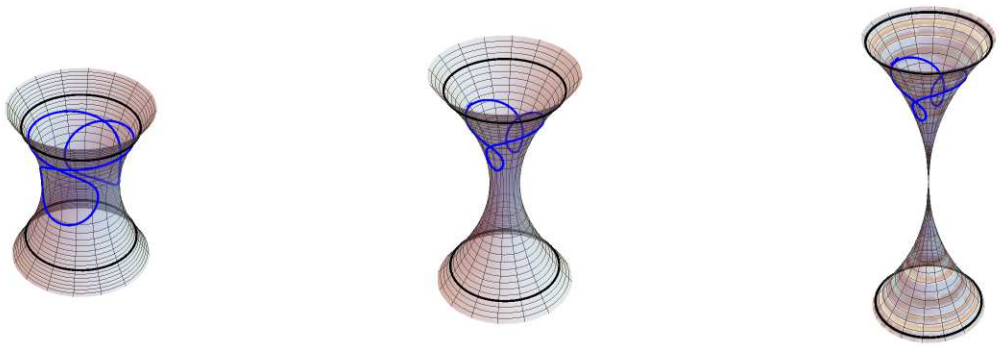

Figure 3.7: Embedding diagram depicting progression of the once-looping MOTS as $T \to 1$. The left-most plot is at $T = 0.8$, the middle is at $T = 0.98$, the right-most is at $T = 1.0$. At $T = 1$ the disconnect of the two asymptotic regions is noted, while the MOTS recedes into the upper region, regions one's black hole interior, as $T \to 1$.

we expect the bridge between the two universes to be closed once $T = 1$ is reached. To aid visually with this, I shall make use of the embedding diagrams described in Section 1.1. These diagrams are useful for describing the behaviours of the MOTSs that I have described within this section.

Figure 3.7 demonstrates the noted closing of the wormhole throat, as well as how the MOTS recede from that closure.

3.3.1 Return Above

For the surfaces that I have presented so far, the throat of the wormhole closing does not result in the surfaces disappearing. Instead, they recede from the throat, and no longer dip into the other universe. This is however not so simple for those surfaces that are not contained in just one region of the Penrose-Carter diagram of the spacetime (Figure 2.7). Considering Figure 3.6 and Figure 3.8, we will not find these surfaces at slices $T \geq 1$ as the wormhole has closed. As one can see from Figure

3.8, the MOTSs are ultimately squeezed about the throat until they can no longer be found.

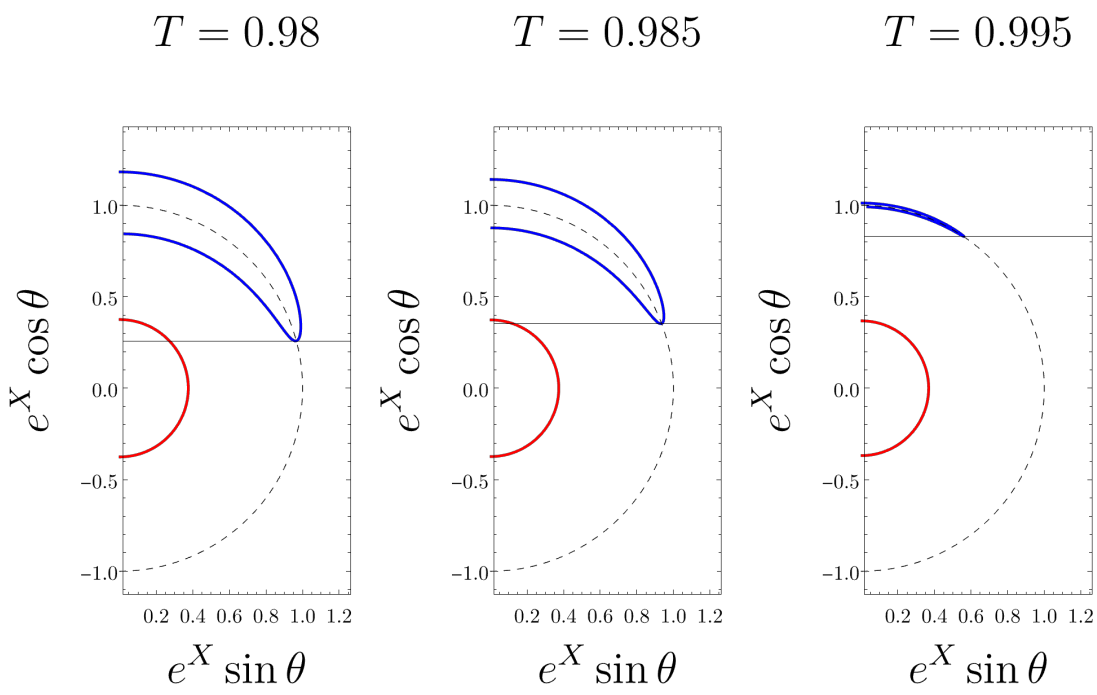

Figure 3.8: MOTS tracked from the $T = 0.98$ slice to the $T = 0.995$ slice. As shown in the figure, the MOTSs area is reduced while approaching $T = 1$ until it apparently vanishes at $T = 1$. It is noted here that the horizontal solid line is used to show where the turn-around happens on the MOTSs, relative to the $e^X \cos\theta$ axis.

This is demonstrated in Figure 3.8 where the MOTS is reduced in area until its disappearance at $T = 1$. This leads to the following conjecture. Any MOTS that behaves in such a way that it closes in a universe in which it did not start, will only exist within the time slices $0 < T \leq 1$.

3.4 Behaviour as $T \to 0$

In previous work [4], it was found that there appear to be an infinite number of MOTSs residing within the horizon of a Schwarzschild black hole solution, within some Painlevé-Gullstrand-like coordinates. In this maximal extension of the Schwarzschild solution, our results suggest that this may be true here as well. However, some discussion is necessary about these results. The defining differential equations are not well-defined on the z-axis, so when utilizing the shooting method we need to be careful in judging whether or not a surface truly closes.

As is seen from Figure 3.9, we find that as $T \to 0$ we can reach a point where we can no longer find closed MOTS within some numerical bound. In other spacetimes it is found that all MOTSs appear to coincide at the moment of time symmetry [11]. This is also the case here as it was found that all surfaces shown within this section, as well as the toroidal surface Section 3.5, all coincide at the same point on the $T = 0$ slice. This is important as it is yet another connection to previous research that has been done on these surfaces in other coordinate choices [4].

3.5 Toroidal MOTSs

One of the most interesting phenomena found while searching for MOTSs within the Kruskal-Szekeres spacetime are toroidal MOTSs. These surfaces are interesting as almost all previously identified exotic MOTSs have been topologically spherical. Toroidal surfaces have been found during numerical simulations of black hole mergers [11], but unlike most of the MOTSs found in previous sections of this paper, they have not been previously found in other exact spacetimes [4, 11].

The first toroidal result is the observation that just like the N-looping surfaces

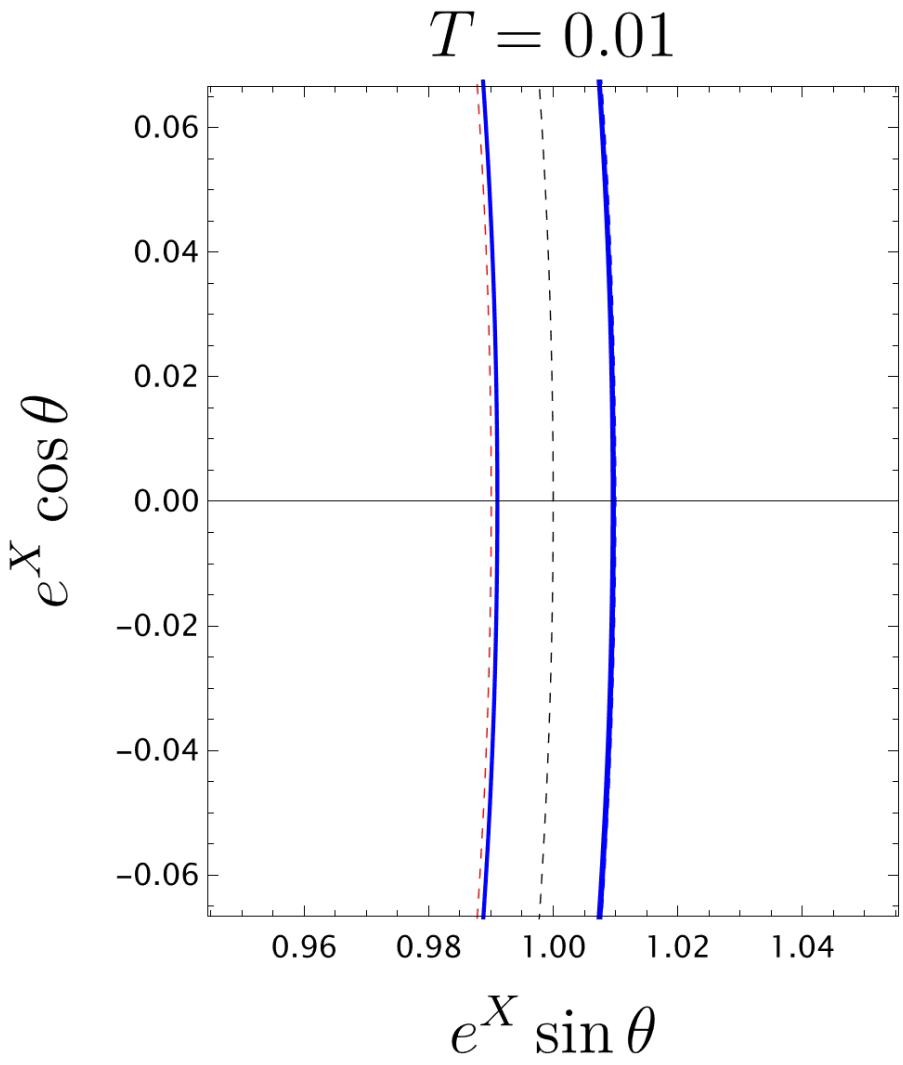

Figure 3.9: Zoomed image of the one-looping MOTS at $T = 0.01$. Here, as in other plots, the blue dashed line is the original universe's black hole horizon, the red dashed line is the other universe's black hole horizon, and the black dashed line is the throat. Plot depicts "squeezed" nature of MOTSs as $T \to 0$.

shown previously, the toroidal MOTSs also coincide at the moment of time symmetry $T = 0$. This brings us to one an interesting result from this work. All MOTSs found within the Kruskal-Szekeres spacetime coincide at $T = 0$.

Similar to how some MOTSs from Section 1.1 behave, the toroidal surfaces we see here do not exist for slices $T \geq 1$. This is due to the fact that all toroidal MOTSs straddle the throat of the wormhole, so unlike some MOTSs, such as those in Figure 3.5, these surfaces can not recede into the black hole once $T = 1$ is reached. Instead the toroidal MOTS contracts towards the throat of the wormhole as $T \to 1$, ultimately ceasing to exist for $T \geq 1$.

Unlike the many N-looping cases found as spherical MOTSs, the surface depicted in Figure 3.10 and Figure 3.11 is the only topologically toroidal MOTS that we have found. No evidence of a toroidal surface that loops itself was found during our analysis. This, along with the different topology of these surfaces, marks these MOTS out as exotic.

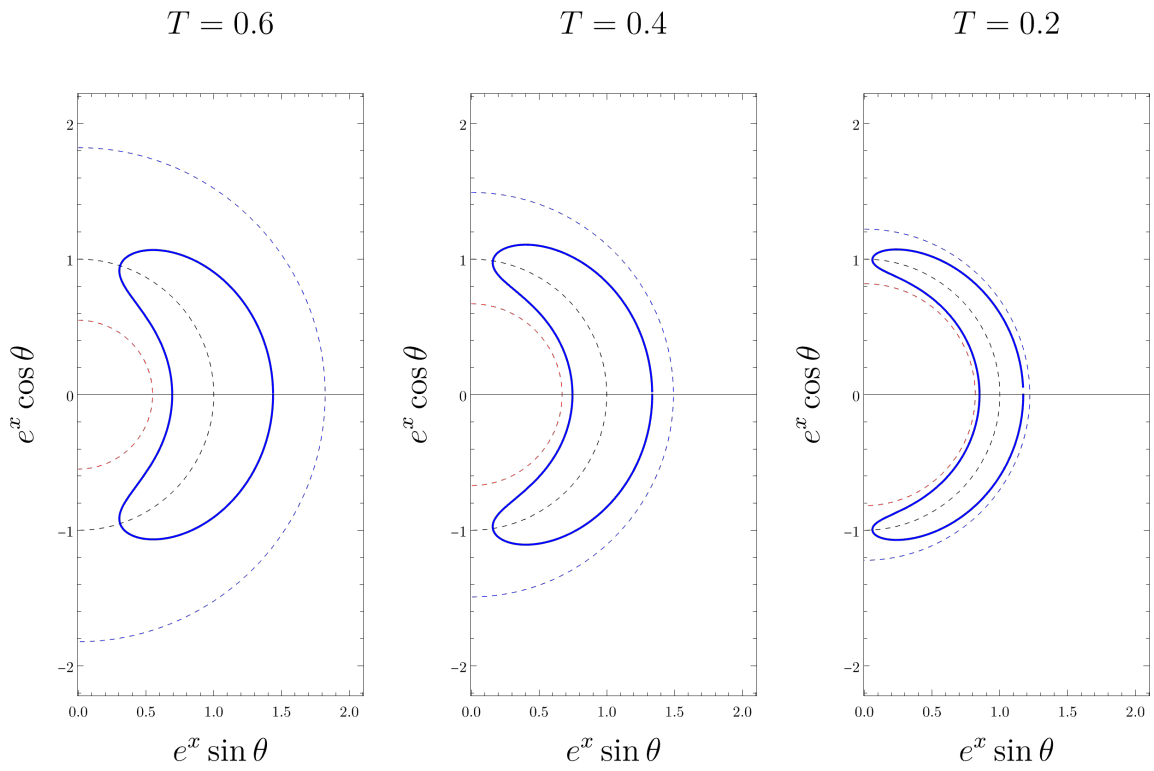

Figure 3.10: The toroidal MOTS progressing from left to right from $T = 0.6$ to $T = 0.2$. Note here that the MOTS is squeezed between the dashed red line and the dashed blue line, which are the other universe's black hole horizon and our universe's black hole horizon respectively. Plots follow the standard plotting scheme for this thesis work.

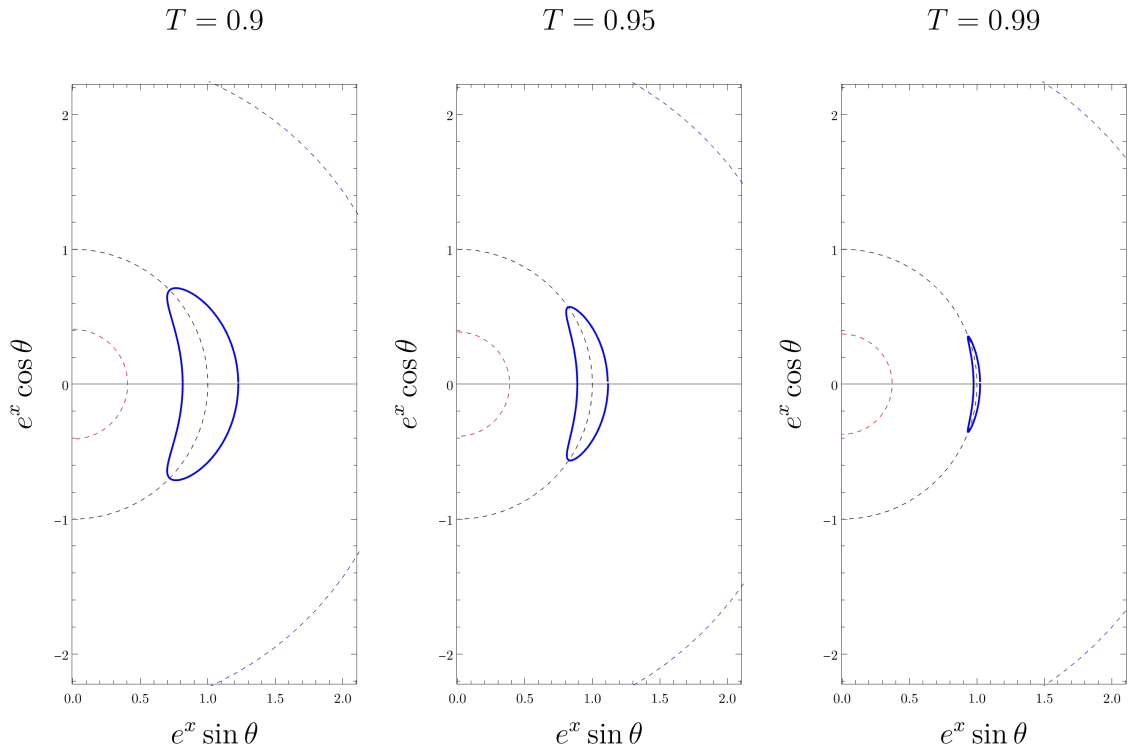

Figure 3.11: The toroidal MOTS progressing from left to right from $T = 0.9$ to $T = 0.99$. Note here that the MOTS straddles the throat of the wormhole, which is the dashed black line. This results in the MOTS only existing for $-1 < T < 1$. Plots follow the standard plotting scheme for this thesis work.

Chapter 4

Stability Operator

When considering the orbit of some object, say some celestial body, a stable orbit is one for which perturbed orbits remain close to the original one. This description of stability may be the first to come to mind when a reader hears "stability of a MOTS", but it is in fact not the correct description of stability for such surfaces. I shall describe what is meant by stability in the context of MOTSs, as well as describe some important observations made while studying such things in the Kruskal-Szekeres extension.

When analyzing the stability of some smooth surface S within a hypersurface Σ, a linear elliptic operator on some function ψ in S is defined by $L_\Sigma \psi = \delta_{\psi m}\theta_\ell$ [1], where $\delta_{\psi m}\theta_\ell$ is the variation of θ_ℓ along ψ_m. On a MOTS, this operator takes the form (4.1) [15]

$$\begin{aligned} L[\psi] &:= -\Delta\psi + 2\omega^A \partial_A \psi + \left[\frac{R^{(2)}}{2} - \frac{1}{2}||\sigma_+||^2 + \mathcal{D}_A\omega^A - ||\omega||^2\right]\psi \\ &= \not{\mathcal{D}}^A \not{\mathcal{D}}_A \psi + \frac{1}{2}\left[R^{(2)} - ||\sigma_+||^2\right]\psi. \end{aligned} \tag{4.1}$$

For an arbitrary surface with $\theta_\ell \neq 0$ additional terms will be present. In this equation $\not{\mathcal{D}} = \mathcal{D}_A - \omega_A$ where $\mathcal{D}_A$ is the covariant derivatives on S and ω_A is defined as (4.2) [8]

$$\omega_B = -\frac{1}{2} e^b_B \ell^-_a \nabla_b \ell^a_+ \,, \tag{4.2}$$

R is the two-dimensional Ricci scalar, $||\sigma_+||^2 = \sigma^{AB}_+ \sigma^+_{AB}$ where σ^+_{AB} is the outward null shear [15]. Relative to the initial data ω_A and σ^+_{AB} can be written as

$$\omega_A = e^i_A K_{ij} \hat{N}^j \tag{4.3}$$

and

$$\sigma^+_{AB} = e^i_A e^j_B (K_{ij} + D_i \hat{N}_j). \tag{4.4}$$

Under the assumption that $\omega = 0$, or in some cases, ω is exact, the stability operator is self-adjoint. This means that the operator has only real eigenvalues. However, in general the operator may have complex eigenvalues [15]. Consider then the following relation,

$$\not{\mathcal{D}}_A (e^\gamma T) = (\mathcal{D}_A - \omega_A)(e^\gamma T) = e^\gamma \mathcal{D}_A T. \tag{4.5}$$

This holds true as long as ω_A takes the form $\omega_A = \mathcal{D}_A \gamma$. With some work, it can be shown from (4.5) that the following is then true,

$$\not{\mathcal{D}}^A \not{\mathcal{D}}_A \psi = e^\gamma \mathcal{D}^A \mathcal{D}_A (e^{-\gamma} \psi). \tag{4.6}$$

Which then lends us the tools required for the rest of this stability work [3, 15],

$$L[\psi] = e^\gamma \bar{L}[e^{-\gamma} \psi], \tag{4.7}$$

where

$$\bar{L} := -\Delta + \frac{1}{2}\left[R^{(2)} - ||\sigma_+||^2\right]. \tag{4.8}$$

This form of the stability operator for $\omega_A = 0$ is self-adjoint, meaning the operator will have real eigenvalues. Then if ψ is an eigenfunction of L with eigenvalue λ,

$$\bar{L}(e^{-\gamma}\psi) = e^{-\gamma}L(\psi) = \lambda e^{-\gamma}\psi. \tag{4.9}$$

That is, $e^{-\gamma}\psi$ is an eigenfunction of $\bar{L}$ with eigenvalue λ. Then L and $\bar{L}$ have the same eigenvalue spectrum and are said to be similar.

In the case of finding the eigenvalue spectrum for the Kruskal-Szekeres spacetime, consider that for the surface generated by rotating the MOTSodesic $(P(s), \Theta(s))$ around the z-axis, while making use of the definition (4.3), ω takes the form

$$\omega = \dot{P}\dot{\Theta}_{r_T}\left(\frac{1}{2}\frac{(N^2)'}{N^2} - 1\right)ds. \tag{4.10}$$

Due to (4.10) being exact, one may study the simpler, similar stability operator of (4.8). To make use of this operator, one must calculate the Laplacian, Ricci curvature, and shear terms. The induced metric on a MOTS (4.11) is

$$q_{AB}dx^A dx^B = ds^2 + q_{\phi\phi}(s)d\phi^2, \tag{4.11}$$

from which we find [15]

$$\begin{aligned}\Delta &= \partial_s^2 + \frac{1}{2}\left(\frac{d}{ds}\log(q_{\phi\phi})\right)\frac{\partial}{\partial s} + \frac{1}{q_{\phi\phi}}\frac{\partial^2}{\partial\phi^2} \\ R^{(2)} &= -\frac{1}{q_{\phi\phi}^{1/2}}\frac{d}{ds}\left(\frac{\dot{q}_{\phi\phi}}{q_{\phi\phi}^{1/2}}\right).\end{aligned} \tag{4.12}$$

The shear term takes the following form,

$$||\sigma^+||^2 = \frac{2(\sigma^+_{\phi\phi})^2}{r^4\sin^4\Theta} \tag{4.13}$$

where

$$\sigma^+_{\phi\phi} = \frac{\sin^2\Theta}{N}(rr_T + r^2 r_X\dot{\Theta}) - \cos\Theta\sin\Theta N r\dot{P}. \tag{4.14}$$

With these equations along with some MOTS solution, the eigenvalue spectrum can now be obtained for such a MOTS by utilizing pseudo-spectral methods [6]. These methods, in this case, begin with considering a solution with an arc length parameterization $s \in [0, s_{max}]$. Then consider the eigenfunctions ψ and expand into Chebyshev polynomials

$$\psi_m(s) = \sum_{n=0}^{N} a_n\phi_n := \sum_{n=0}^{N} a_n\cos\left(\frac{n\pi s}{s_{max}}\right). \tag{4.15}$$

The interval $[0, s_{max}]$ is then placed on a uniform grid of $N+1$ points. Next, a matrix representation of the system is constructed and takes the following form,

$$\bar{L}[\psi] = \lambda\psi \rightarrow \bar{L}_{ij}a_j = \lambda\Phi_{ij}a_j, \tag{4.16}$$

with $\bar{L}_{ij} = (\bar{L}_\Sigma\phi_j)(s_i)$ and $\Phi_{ij} = \phi_j(s_i)$. Finally, the eigenvalue spectrum is found for $M = \Phi^{-1}L$ with built-in Mathematica packages.

One may question the numerical stability of such solvers, so I will provide a brief explanation of the numerical checks made to ensure proper solutions. Quite simply, at every eigenvalue solve for some matrix of size $(N \times N)$, a check is made by solving for the same system at a matrix size of $(N+1) \times (N+1)$. If the solution differs by more than some preset tolerance, a larger initial matrix size will be used. As noted in [11], matrix sizes of $N = 100$ are sufficient for achieving an accepted convergence.

Ultimately, the goal of using this operator is to obtain information about the nature of the associated MOTSs. The eigenvalue spectrum of the operator specifically holds the important information. In general, if $\omega \neq 0$ the spectrum of eigenvalues for the stability operator is not strictly real, however, all considered in this thesis are real. From [1], the eigenvalue with the smallest real part is the *principal eigenvalue* and this component specifically holds information about the nature of the stability of the analyzed MOTS. If the principal eigenvalue λ_0 is positive, that is $\lambda_0 > 0$, the MOTS is said to be *strictly stable*. Strictly stable implies that the MOTS can be uniquely evolved forwards and backwards in time, as well as being a boundary between trapped and untrapped regions: Small outward deformations of the MOTS are outer untrapped while small inward ones are outer trapped. If $\lambda_0 \geq 0$ the surface is just said to be stable. If $\lambda_0 < 0$, the surface is unstable: there exist outer trapped surfaces outside the MOTS and outer untrapped ones inside. As in a plethora of similar works [4], the vast majority of MOTSs studied in this work are not spherically symmetric and are therefor unstable [3]. Unstable here means that the surfaces are no longer boundaries between trapped and untrapped regions but does not mean that these surfaces do not serve in some purpose. In fact, unstable surfaces aid in our understanding of horizon dynamics, as they are a key part in understanding the annihilating/bifurcating nature of horizons within black hole merger simulations [13].

I shall now present some of the results found when studying this operator for

surfaces that we found in the Kruskal-Szekeres time slices, as well as comparing the results to previously done stability operator works. As discussed throughout the course of this thesis, there are many similarities between the N-looping MOTSs found in the Kruskal-Szekeres slices of Schwarzschild and those within other time slices such as Painlevé-Gullstrand. The results found while studying surfaces within Painlevé-Gullstrand-like slicings of assorted spherical spacetimes showed that the principle eigenvalue of all MOTSs aside from the outer-most horizon was negative, meaning they are all unstable [11]. It was hypothesized that the N-looping surfaces in the Kruskal-Szekeres coordinates would certainly follow the same behaviour of those in Painlevé-Gullstrand and that is precisely what was found.

What was not known however, was the nature of stability for the toroidal MOTS as such surfaces had not previously been studied in exact solutions. By examining Figure 4.2 it is found that we have the same result as the N-looping MOTSs, instability. Yet again, it is found that the only strictly stable MOTS in the spacetime is the outer-most horizon.

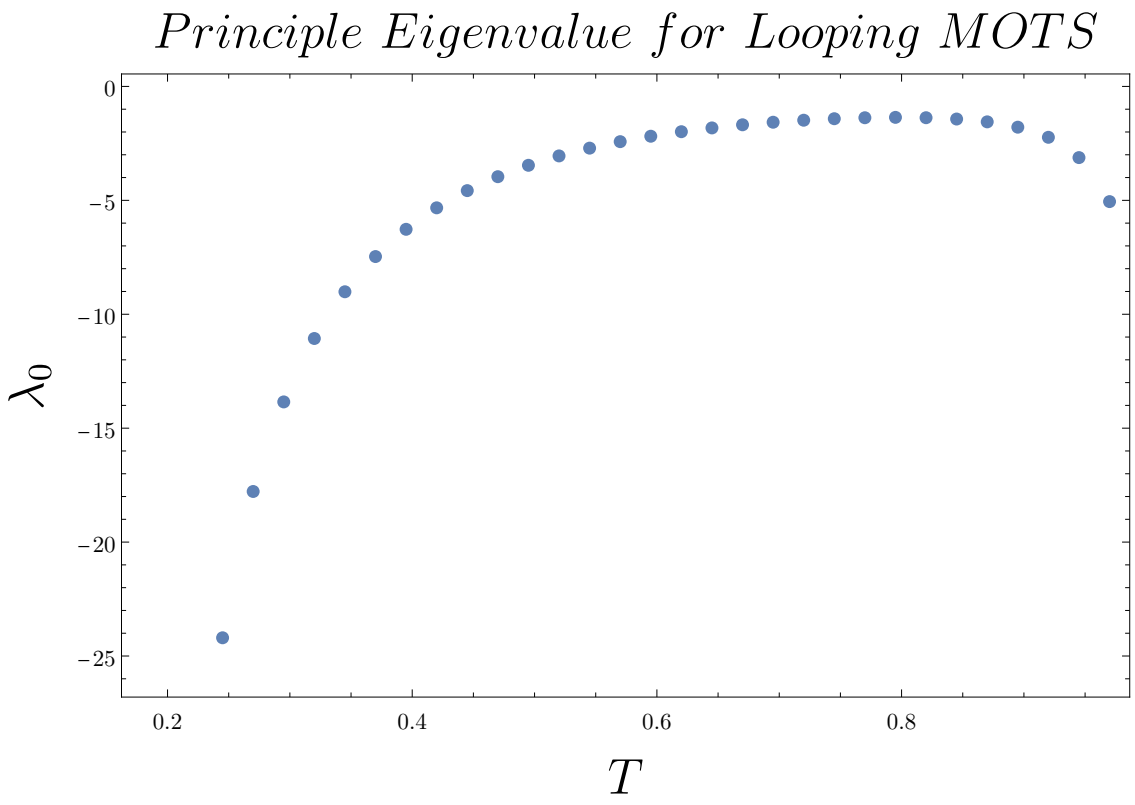

Figure 4.1: Principle eigenvalue for the once-looping MOTS, plotted from approximately $T = 0.1$ to $T = 1.0$. Negative values shown at every point for the once-looping surface, indicating that the surface is unstable at all points.

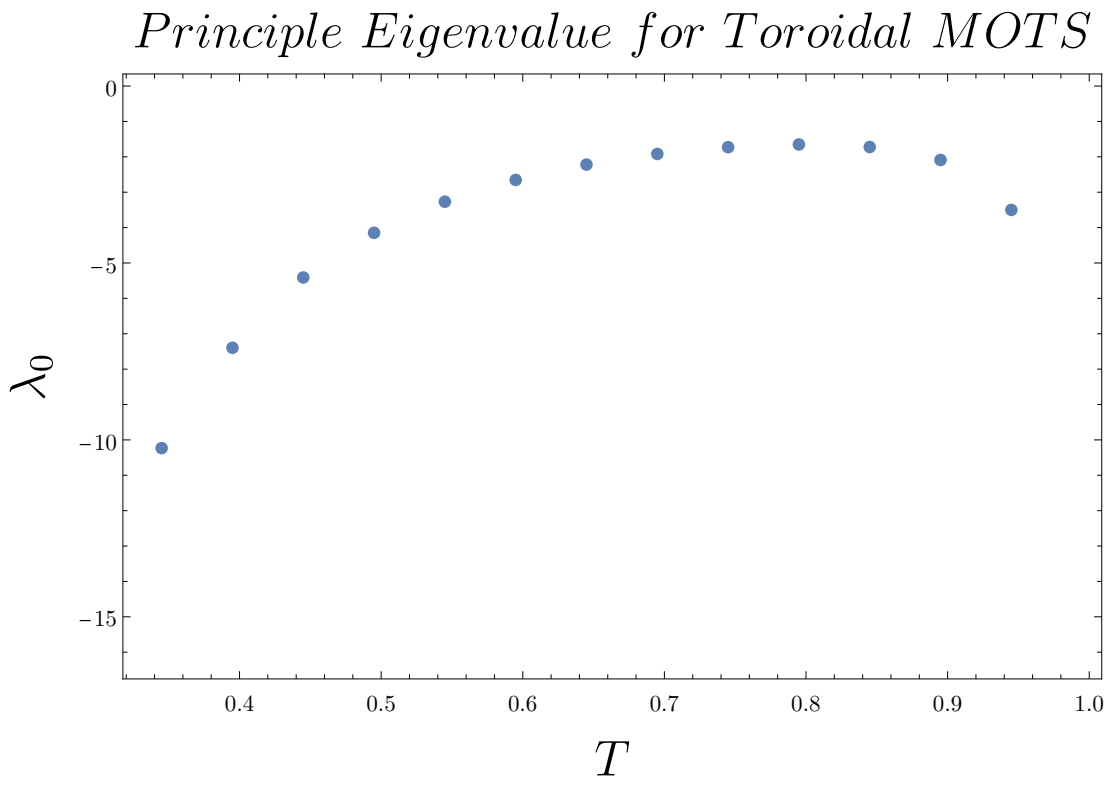

Figure 4.2: Principle eigenvalue for the toroidal MOTSs for T values of $T \approx 0.3$ to $T \approx 1.0$. Plot indicates negative eigenvalue for all values of T for the toroidal MOTS, hence the surface is unstable.

Chapter 5

Conclusion

Throughout this thesis MOTS have been discussed from several perspectives. From the initial descriptions of apparent horizons from Hawking and Ellis [10], to the descriptions of attributes these surfaces have, such as their eigenvalue spectra, these surfaces have been studied and analyzed extensively within the context of the maximal Schwarzschild extension. I have shown, through this study, the connections observed between this maximal extension of the Schwarzschild coordinates and other coordinates studied in a similar manner, such as the Painlevé-Gullstrand coordinates [4], or the Reissner-Nordström spacetime. The number of similarities that are noted are indeed plentiful, such as the self-intersecting, or looping, MOTS sharing quite a large number of similar key behaviours between several different coordinate time slicings. An example that stands out is that in all of the studies that share a similar method and system to this thesis work [4, 11], all surfaces coincide at the moment of time symmetry.

There are however some differences that have been noted, such as the toroidal MOTS. While the MOTSs that have exotic behaviours about the throat, like the "fang-like" MOTSs (Figure 3.8), are interesting, the toroidal surfaces are of greater

interest here for a few reasons. The first reason is that these surfaces have only been found in the Kruskal-Szekeres coordinates, along with the merger simulations I have noted previously [4]. The other key reason is that the toroidal surfaces straddle the throat of the wormhole, ceasing to exist once the throat is closed at slices $T > 1$.

I have also shown that through methods previously used in [1, 15, 8], one can find the eigenvalue spectra for these surfaces and make use of the principal eigenvalue to obtain information about the geometry of the surface itself. Comparing with those works, yet another connection is shown between the Kruskal-Szekeres coordinates and its cousins: all surfaces except from the outer-most horizon are unstable, including the toroidal MOTS. This is one of the main discoveries associated with the works which preceded this thesis. The toroidal MOTS were found previously in black hole merger simulations like that in [12]. Now that these toroidal surfaces have been found in a study considering only one black hole and not a merger event, the following can be stated. Toroidal surfaces are not strictly a consequence of a merger event. Instead, it appears that they are associated with the departure from the moment of time symmetry, the same as all other MOTSs found.

Ultimately, the results from this thesis contribute to the ever expanding studies of black hole horizon behaviours. While there is not much known as to the physical consequences of these surfaces, one goal of studying these MOTSs is to aid in our understanding of the interior black hole horizon dynamics and perhaps find connections to the outer-most black hole horizons and the attributes from those horizons that may correlate with effects in the spacetime outside of the black hole. There is evidence to believe that tracking these MOTSs along with their associated eigenvalue spectra may aid in the mapping of what is called "bifurcation/annihilation events" [11], which are specifically points in the evolution of these systems where horizons appear or disappear. This work is another step in the ladder that leads toward understanding

these interior black hole dynamics and their connections.

Bibliography

[1] Lars Andersson, Marc Mars, and Walter Simon. "Local Existence of Dynamical and Trapping Horizons". In: *Physical Review Letters* 95.11 (Sept. 2005). ISSN: 1079-7114. DOI: 10.1103/physrevlett.95.111102. URL: http://dx.doi.org/10.1103/PhysRevLett.95.111102.

[2] Thomas W. Baumgarte and Stuart L. Shapiro. *Numerical Relativity: Starting from Scratch*. Cambridge University Press, Feb. 2021. ISBN: 978-1-108-93344-5, 978-1-108-84411-6, 978-1-108-92825-0. DOI: 10.1017/9781108933445.

[3] Ivan Booth, Graham Cox, and Juan Margalef-Bentabol. "Symmetry and instability of marginally outer trapped surfaces". In: *Classical and Quantum Gravity* 41.11 (May 2024), p. 115003. ISSN: 1361-6382. DOI: 10.1088/1361-6382/ad3dab. URL: http://dx.doi.org/10.1088/1361-6382/ad3dab.

[4] Ivan Booth, Robie A. Hennigar, and Saikat Mondal. "Marginally outer trapped surfaces in the Schwarzschild spacetime: Multiple self-intersections and extreme mass ratio mergers". In: *Physical Review D* 102.4 (Aug. 2020). ISSN: 2470-0029. DOI: 10.1103/physrevd.102.044031. URL: http://dx.doi.org/10.1103/PhysRevD.102.044031.

[5] Ivan Booth et al. "Exotic marginally outer trapped surfaces in rotating spacetimes of any dimension". In: *Classical and Quantum Gravity* 40.9 (Apr. 2023),

p. 095010. ISSN: 1361-6382. DOI: 10.1088/1361-6382/acc306. URL: http://dx.doi.org/10.1088/1361-6382/acc306.

[6] John Boyd, To Marilyn, and Paraphrasing Eliot. "Chebyshev and Fourier Spectral Methods". In: (Oct. 2000).

[7] Albert Einstein. *Relativity: The Special and General Theory*. Routledge, 1921.

[8] P. Hájıček. "Three remarks on axisymmetric stationary horizons". en. In: *Comm. Math. Phys.* 35.1 (1974), pp. 305–320. URL: http://dml.mathdoc.fr/item/1103859774.

[9] J. B. Hartle. *Gravity: An introduction to Einstein's general relativity*. 2003. ISBN: 978-0-8053-8662-2.

[10] S. W. Hawking and G. F. R. Ellis. *The Large Scale Structure of Space-Time*. Cambridge Monographs on Mathematical Physics. Cambridge University Press, 1973.

[11] Robie A. Hennigar et al. *The Interior MOTSs of Spherically Symmetric Black Holes*. 2021. arXiv: 2111.09373 [gr-qc].

[12] Daniel Pook-Kolb, Ivan Booth, and Robie A. Hennigar. "Ultimate fate of apparent horizons during a binary black hole merger. II. The vanishing of apparent horizons". In: *Physical Review D* 104.8 (Oct. 2021). ISSN: 2470-0029. DOI: 10.1103/physrevd.104.084084. URL: http://dx.doi.org/10.1103/PhysRevD.104.084084.

[13] Daniel Pook-Kolb et al. "Interior of a Binary Black Hole Merger". In: *Phys. Rev. Lett.* 123 (17 Oct. 2019), p. 171102. DOI: 10.1103/PhysRevLett.123.171102. URL: https://link.aps.org/doi/10.1103/PhysRevLett.123.171102.

[14] Karl Schwarzschild. "On the gravitational field of a mass point according to Einstein's theory". In: *Sitzungsber. Preuss. Akad. Wiss. Berlin (Math. Phys.)* 1916 (1916), pp. 189–196. arXiv: physics/9905030.

[15] Kam To Billy Sievers et al. "Marginally outer trapped tori in black hole spacetimes". In: *Physical Review D* 109.12 (June 2024). ISSN: 2470-0029. DOI: 10.1103/physrevd.109.124023. URL: http://dx.doi.org/10.1103/PhysRevD.109.124023.

[16] K. Srinivasa Rao. *The rotation and Lorentz groups and their representations for physicists*. eng. New York ; Wiley, 1988. ISBN: 0470210443.